

Texture, geochemistry, and geochronology of titanite and pyrite: Fingerprint of magmatic-hydrothermal fertile fluids in the Jiaodong Au province

XING-HUI LI^{1,2}, HONG-RUI FAN^{1,2,3,*}, RI-XIANG ZHU^{2,3,4}, MATTHEW STEELE-MACINNIS⁵,
KUI-FENG YANG^{1,2,3,†}, AND CAI-JIE LIU⁶

¹Key Laboratory of Mineral Resources, Institute of Geology and Geophysics, Chinese Academy of Sciences, Beijing 100029, China

²Innovation Academy for Earth Science, Chinese Academy of Sciences, Beijing 100029, China

³College of Earth and Planetary Science, University of Chinese Academy of Sciences, Beijing 100049, China

⁴State Key Laboratory of Lithospheric Evolution, Institute of Geology and Geophysics, Chinese Academy of Sciences, Beijing 100029, China

⁵Department of Earth and Atmospheric Sciences, University of Alberta, Edmonton, Alberta T6G 2E3, Canada

⁶No. 6 Institute of Geology and Mineral Resources Exploration of Shandong Province, Zhaoyuan 265400, China

ABSTRACT

The Au mineralization in the giant Jiaodong Au province is enigmatic and difficult to fit current classic mineralization models, primarily because of uncertainties as to the sources of ore-forming fluids and metals. The ca. 120 Ma Au mineralization has been previously proposed to have occurred during a magmatic lull, which would negate a magmatic-hydrothermal genetic model. However, recent drilling has revealed a buried mineralized monzonite equivalent in age to the Au mineralization in the Linglong goldfield. Here, we present comprehensive textural, geochemical [LA-(MC)-ICP-MS trace element, Nd and S isotopes] and geochronological (LA-ICP-MS U-Pb dating) analyses of titanite and pyrite from this previously unrecognized monzonite. Three types of titanite were distinguished, including magmatic Ttn1 and hydrothermal Ttn2 and Ttn3, which show indistinguishable U-Pb ages (120.7 ± 3.1 and 120.9 ± 2.6 Ma), REE patterns and Nd isotopes [$\epsilon_{Nd}(t) = -14.7$ to -12.9], implying that hydrothermal fluids were directly exsolved from the monzonitic magma, contemporaneous with the large-scale Au mineralization at ca. 120 Ma. The Nd isotopes of titanite potentially indicate a lower crustal source mixed with mantle materials for the monzonite. Four types of pyrite were analyzed, including magmatic Py1 from fresh biotite monzonite, hydrothermal Py2 from altered biotite monzonite, hydrothermal Py3 from quartz-pyrite veins with a monazite U-Pb age of 118.2 ± 4.6 Ma, and magmatic Py4 from mafic enclaves of the Gushan granite at ca. 120 Ma. The $\delta^{34}\text{S}$ values of magmatic Py1 and Py4 (+1.9 to +6.3‰, and +5.0 to +6.4‰, respectively) and hydrothermal Py2 and Py3 (+6.4 to +9.5‰ and +6.5 to +7.6‰, respectively) are consistent with sulfur isotopic fractionation between melt and fluid. Hydrothermal Py2 and Py3 also have higher Co, As, Ag, Sb, and Bi contents and submicrometer gold inclusions, implying that the magmatic-hydrothermal fluids were fertile for mineralization. This study highlights the importance of monzonite magmatism and exsolved fertile fluids in regional Au mineralization. Hydrous magmas at ca. 120 Ma probably extracted Au efficiently from the lower crustal-mantle sources and released auriferous fluids at the late magmatic stage, leading to the formation of Au deposits in the Jiaodong province.

Keywords: Titanite, pyrite, monazite, biotite monzonite, U-Pb geochronology, magmatic-hydrothermal fluid

INTRODUCTION

The Early Cretaceous Au deposits in the Jiaodong Peninsula constitute the largest Au province of China, containing more than 5000 tons of proven Au resources. Mineralization in the Jiaodong Peninsula is considered unique relative to the accepted model for orogenic Au deposits (e.g., Groves et al. 1998), in that Au mineralization postdates the Precambrian metamorphic wall rocks by about 2 billion years (Goldfarb and Santosh 2014). Numerous studies have defined the ore-controlling structures, hydrothermal alterations, ore-fluid chemistry, hydrothermal processes, and fluid evolution of both disseminated- to stockwork-style

and auriferous quartz-pyrite vein-type Au deposits across the Jiaodong Peninsula (Fan et al. 2003, 2007; Li et al. 2012a, 2018; Goldfarb and Santosh 2014; Mills et al. 2015; Deng et al. 2015, 2020b; Feng et al. 2018, 2020). The timing of Au mineralization has also been well constrained to 120 ± 5 Ma by Rb-Sr dating of pyrite, $^{40}\text{Ar}/^{39}\text{Ar}$ dating of hydrothermal muscovite and U-Pb dating of hydrothermal monazite (Yang and Zhou 2001; Ma et al. 2017; Li et al. 2018; Zhang et al. 2020; Deng et al. 2020a). Nevertheless, the genesis of the Jiaodong Au province is contentious, given the failure of current models of mineralization to account for its features. This debate is primarily rooted in uncertainties as to the sources of ore-forming fluids and metals, and particularly their genetic relationship(s) to Mesozoic magmatism, Precambrian metamorphic host rocks, subducted slab and sediment, and/or metasomatized lithosphere (Zhai et al. 2004;

* E-mail: fanhr@mail.iggcas.ac.cn. Orcid 0000-0002-3816-1606

† Orcid 0000-0003-1997-318X

Chen et al. 2005; Goldfarb and Santosh 2014; Zhu et al. 2015; Deng et al. 2015, 2020b; Wang et al. 2020).

Two main problems obstruct linking Au mineralization to the widespread granitic magmatism in the Jiaodong Au province. First, a time gap of at least ~8 million years separates the ages of mineralization and of known magmatism (Li et al. 2019a; Deng et al. 2020a). Second, direct evidence for a genetic affinity between magmatism and hydrothermal mineralization has been hitherto lacking. However, recent deep drilling projects in the Linglong goldfield, one of the largest Au-producing districts in the Jiaodong Au province, discovered a buried mineralized biotite monzonite that shows petrographic features distinct from those of the exposed Mesozoic granitoids (Linglong, Luanjiahe, Guojialing, and Aishan granites). Shen et al. (2016) constrained the emplacement age of the monzonite to ca. 124 Ma by $^{40}\text{Ar}/^{36}\text{Ar}$ dating of biotite and suggested a temporal relationship between the monzonite and Au mineralization. The monzonite is nearly contemporaneous with the regional Gushan granite, which has a zircon U-Pb age of 120–119 Ma (Li et al. 2012b). Thus, this newly discovered monzonite suggests a potentially extensive episode of magmatism during this period. Moreover, the mineralized monzonite shows distinctive hydrothermal features, suggesting a relationship between magmatic-hydrothermal fluids and mineralization. As such, the mineralized monzonite provides a good opportunity to evaluate the role of magmatism and magmatic-hydrothermal fluid release in the ore-forming process, and to explore the sources of ore-forming fluids and metals, in the Jiaodong Au province.

Several magmatic-hydrothermal minerals are present in the monzonite, including titanite, monazite, pyrite, pyrrhotite, and magnetite. Titanite commonly contains sufficient uranium contents for precise U-Pb dating and has been widely used to date magmatic and hydrothermal events (Frost et al. 2001; Li et al. 2010; Xiao et al. 2021). Incorporation of minor and trace elements, such as V, Mn, Cu, Zr, REE, Hf, Pb, Th, and U, into titanite is sensitive to temperature, pressure, oxygen fugacity, and melt and fluid compositions. As such, titanite can be a valuable indicator of magmatic and hydrothermal conditions (Hayden et al. 2008; Xie et al. 2010; Cao et al. 2015; Xiao et al. 2021). The trace elements and sulfur isotopes of pyrite and pyrrhotite can be used to discriminate different sulfur sources and genetic environments, and to understand the physicochemical conditions of sulfide deposition (Deditius et al. 2014; Peterson and Mavrogenes 2014; Tanner et al. 2016; Li et al. 2018). Similarly, magnetite is stable over a wide range of magmatic-hydrothermal conditions and has been used to derive insights on petrogenetic discrimination, physicochemical conditions, and the magma fertility (Dare et al. 2014; Zhi et al. 2019; Dora et al. 2020). The geochemistry of these magmatic-hydrothermal minerals, when integrated with detailed microtextural studies, is useful in fingerprinting magmatic and hydrothermal processes.

Here, we document results of detailed textural studies, in situ U-Pb geochronology and trace-element and isotope geochemistry of magmatic-hydrothermal titanite, monazite, pyrite, pyrrhotite, and magnetite from the mineralized biotite monzonite, as well as pyrite in mafic enclaves from the Gushan pluton. Our results provide insight into (1) the temporal relationship between the monzonite and Au mineralization;

(2) the link between magmatic and hydrothermal events; (3) the mineralization potential of the monzonite; and (4) the sources of the ore-forming fluids and metals in the Jiaodong Au province.

GEOLOGIC BACKGROUND

Regional geology

The Jiaodong Peninsula is located at the southeastern margin of the North China Craton (NCC), bounded by the crustal-scale Tancheng-Lujiang (Tan-Lu) fault to the west. The peninsula comprises the Jiaobei Terrane in the northwest and the Sulu ultrahigh-pressure (UHP) metamorphic belt in the southeast, which are separated by the Wulian-Yantai Fault (Zhou et al. 2008; Fig. 1). The northern Jiaobei Uplift on the Jiaobei Terrane is dominated by Precambrian metamorphic basement, including the Neoproterozoic Jiaodong Group, the Paleoproterozoic Jingshan and Fenzishan Groups, and the Neoproterozoic Penglai Group. These rocks were intruded by widespread middle-late Mesozoic granitoids [the Jurassic Linglong and Luanjiahe granite at 160–159 Ma, the Cretaceous Guojialing granodiorite at 130–126 Ma, Gushan granite at 120–119 Ma, and Aishan-Sanfoshan granite at 118–115 Ma (Miao et al. 1997; Goss et al. 2010; Li et al. 2012b, 2019a; Yang et al. 2012; Fig. 1)], whereas the southern Jiaolai Basin is filled with Cretaceous sedimentary and volcanic rocks (Liu et al. 2009; Xie et al. 2012). The Sulu UHP belt mainly consists of Neoproterozoic granitic gneisses, Triassic UHP metamorphic rocks, and Jurassic-Cretaceous granitoids (Zheng 2008; Xu et al. 2016). Structurally, the Jiaodong Peninsula is dominated by northeast (NE) to north-northeast (NNE) trending brittle-ductile shear zones with sinistral-oblique-reverse movements in the Late Jurassic, followed by late reactivation and development of brittle normal faults in the Early Cretaceous (Sun et al. 2007; Deng et al. 2015).

Deposits in the Jiaodong Au province are divided into three belts from west to east: the Zhaoyuan-Laizhou, Penglai-Qixia, and Muping-Rushan belts. The deposits are distributed along regional second- or third-order NE- to NNE-trending faults of the Tan-Lu fault system, particularly the Sanshandao-Cangshang, Jiaojia-Xincheng, Zhaoyuan-Pingdu, Qixia, and Muping-Rushan faults (Fig. 1; Fan et al. 2007). The majority of Au deposits, dated at 120 ± 5 Ma, are hosted within the widespread Jurassic Linglong, Luanjiahe and Kunyushan granites, Cretaceous Guojialing granodiorite, and Precambrian metamorphic rocks (e.g., Yang and Zhou 2001; Fan et al. 2003; Li et al. 2012a, 2018; Zhang et al. 2020; Deng et al. 2020a). Quartz-sulfide vein-type and disseminated/stockwork-type Au mineralization account for most of the Au resources in the Jiaodong Au province. These deposits are thought to have formed within the same tectonic setting but under different local stress fields (Qiu et al. 2002; Yang et al. 2018). Of the three belts, the Zhaoyuan-Laizhou belt is the most significant in terms of endowment, hosting over 85% of Au resources in the district.

Ore geology and petrography

The Linglong goldfield, which contains several large Au deposits such as Linglong, Jiuqu, and Dongfeng, is located to the east of the Zhaoyuan-Laizhou Au belt and at the northern tip of the Zhaoyuan-Pingdu fault (Fig. 1). This goldfield is typified by the quartz-sulfide vein-type mineralization, with minor disseminated sulfide replacements and stockworks. Hundreds of auriferous

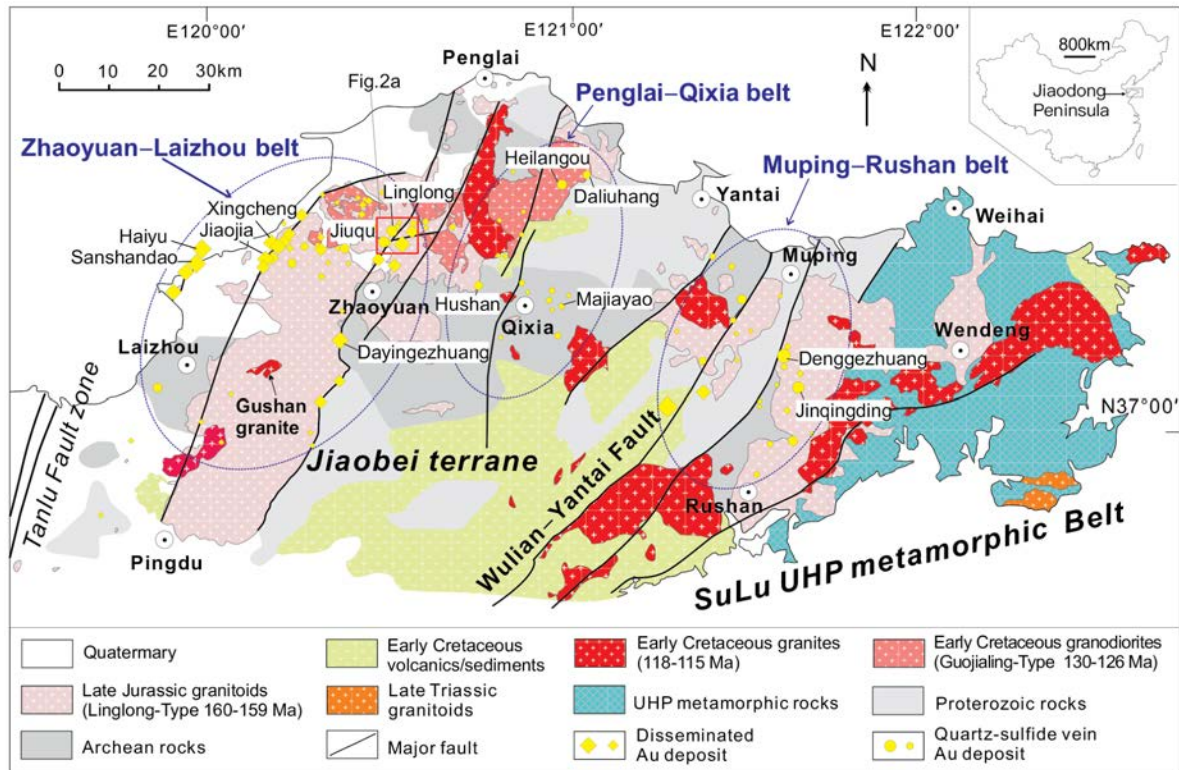


FIGURE 1. Geological map showing the distribution of basement rocks, UHP metamorphic rocks, Mesozoic igneous rocks, and Au deposits in the three Au belts of the Jiaodong Au province. Modified after Yang et al. (2012). (Color online.)

quartz veins are present in this goldfield, occurring in steeply dipping, NE- to NNE-trending fractures in the hanging wall of the Zhaoyuan-Pingdu fault. The mineralized veins are mainly hosted in the Jurassic Linglong and Luanjiahe granites, with fewer in the Cretaceous Guojialing granodiorite (Wen et al. 2015). The Zhaoyuan-Pingdu fault is intersected by the NEE-trending Potouqing fault and crosscut by the NNE-trending Linglong fault, both of which control the occurrence of ore bodies and the widespread emplacement of intermediate to mafic dikes.

The mineralized biotite monzonite was found in drill cores 72ZK1 and 72ZK2, at depths of 2070 and 2374 m separately in the Linglong goldfield, and was suggested as a buried intrusion into the Jurassic Linglong and Luanjiahe granite (Fig. 2; Shen et al. 2016). The biotite monzonite is dark gray to light grayish-green, massive, and medium to fine grained. Pyrite, pyrrhotite, and magnetite are evenly distributed in the monzonite, with some grains occurring as clusters (Figs. 3a–3d and 3g). The mineral assemblage of the monzonite mainly comprises K-feldspar (35–40%), plagioclase (20–25%), and biotite (15–20%) (Figs. 3g and 3h). Other minerals include quartz (5–10%), amphibole (<5%), titanite, and minor zircon, allanite, and apatite. Some coarse grains of K-feldspar and plagioclase have been altered to clay minerals, sericite and chlorite (Fig. 3h).

Silicification, sericitization, and carbonation occurred in the biotite monzonite near the intrusive contact with the overlying Jurassic Luanjiahe granite, whereas unaltered rocks were present at greater depth. The alteration is characterized mostly by addition of quartz, sericite, chlorite, and calcite. Several quartz-pyrite

veinlets are observed in the overlying Luanjiahe granite (Fig. 3e), suggesting a hydrothermal event probably related to the emplacement and degassing of the monzonitic magma.

The Gushan granite, located in the southwest of the Linglong goldfield, ~35 km away from the drill core 72ZK1 (Fig. 1), intrudes the Jurassic Luanjiahe granite and carries mafic microgranular enclaves (MMEs, Fig. 3f). The MMEs are generally fine-grained and contain dominantly hornblende, plagioclase, biotite, K-feldspar, and quartz, with minor apatite and titanite. Some pyrite crystals, co-existing with magnetite and chalcopyrite, are found in the MMEs.

SAMPLES AND ANALYTICAL METHODS

Representative samples were collected from the drill core 72ZK1 in the Linglong goldfield, including quartz-pyrite veinlets (19ZY09), silicified-sericitized-carbonated monzonite (19ZY01, 19ZY07, 19ZY13, 19ZY15), and fresh to weakly altered biotite monzonite (19ZY03, 19ZY14) at depths 2056–2153 m. Samples of MMEs from the Gushan pluton were also analyzed. Petrographic studies were carried out on thin sections using field emission scanning electron microscope (FESEM). Titanite and hydrothermal monazite were analyzed for geochronology, major and trace element contents, and Nd isotopes using EPMA, LA-ICP-MS, and LA-MC-ICP-MS. Pyrite, pyrrhotite, and magnetite were selected for in situ trace elemental and/or sulfur isotopic analyses using LA-ICP-MS and LA-MC-ICP-MS. Except for FESEM and EPMA analyses, which were done at the Institute of Geology and Geophysics, Chinese Academy of Sciences (IGGCAS), other measurements were all conducted at the Wuhan Sample Solution Analytical Technology Co., Ltd., China.

In situ titanite U-Pb dating and geochemical analyses

The major element compositions of titanite were determined using a JEOL-JXA8100 electron microprobe. The operating conditions were 15 kV accelerating voltage, 10 nA beam current, and 5 μ m probe beam. Calibration standards used were diopside for Ca and Si, jadeite for Al and Na, garnet for Fe, bustamite for

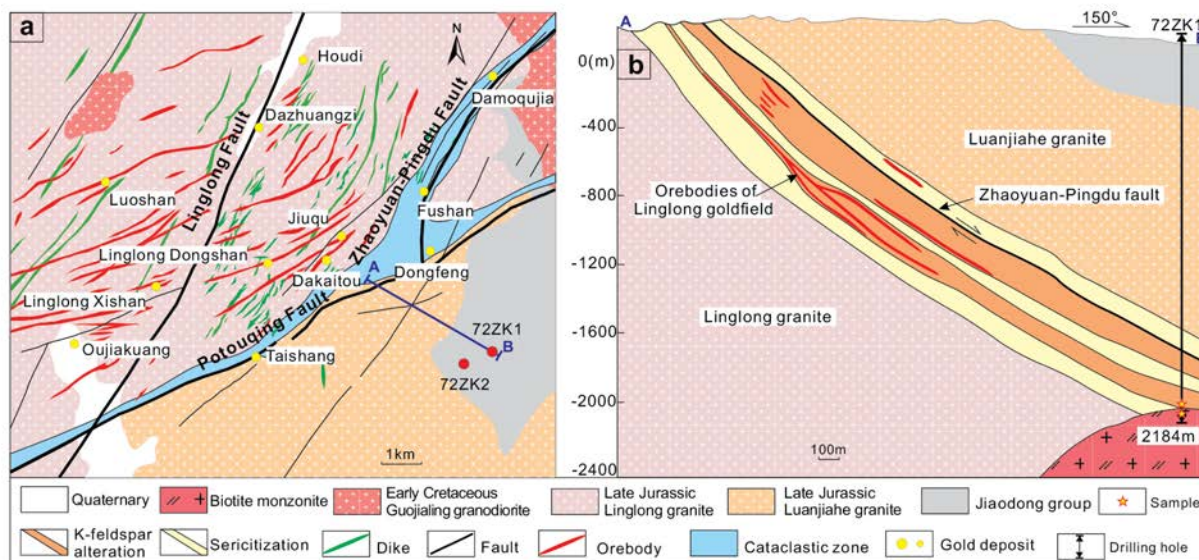


FIGURE 2. (a) Geologic map of the Linglong goldfield, showing the distribution of orebodies, modified after Wen et al. (2015). (b) Cross section of the Line 72 in the Linglong goldfield and sample location. (Color online.)

Mn, K-feldspar for K, tugtupite for Cl, and fluorite for F. The data were corrected using the atomic number-absorption-fluorescence (ZAF) method.

Prior to analytical works, titanite grains were carefully examined using transmitted and reflected light microscopy and backscatter electron (BSE) images so as to avoid fractures, inclusions, and U-rich domains. In addition, magmatic and hydrothermal titanites were distinguished preliminarily based on their occurrence, texture (oscillatory vs. core-rim and irregular zoning), and mineral association. In situ U-Pb isotopes and trace elements of titanite were analyzed simultaneously by LA-ICP-MS employing an Agilent 7900 ICP-MS with a Geolas HD laser ablation system. A spot size of 44 μm was used with a pulse rate of 3 Hz and laser energy of 80 mJ. The Pb/U ratios were calibrated against the zircon standard 91500 (Wiedenbeck et al. 1995) and monitored according to the titanite standard MKED1 (Spandler et al. 2016). NIST 610 was used as an external standard, and average CaO concentrations of titanite determined by EPMA were used as the internal standard. Each analysis incorporated a background acquisition of ~20 s followed by 50 s of data acquisition. Details of the operating conditions, analytical method, and data reduction process can be found in Liu et al. (2008). A Microsoft Excel-based spreadsheet ICP-MSDataCal was used to perform off-line selection and integration of background and analyzed signal, time-drift correction, and quantitative calibration for U-Pb dating and trace element analysis (Liu et al. 2008). Tera-Wasserburg Concordia diagrams and weighted mean calculations were made using Isoplot/Ex_ver3 (Ludwig 2003).

In situ Nd isotopes of titanite were measured on spots previously analyzed for U-Pb dating using a Neptune Plus multi-collector ICP-MS, coupled with a Geolas HD excimer ArF laser ablation system. A laser pulse energy of ~90 mJ, repetition rate of 8 Hz, and spot size of 32 μm were used. The mass discrimination factor for $^{143}\text{Nd}/^{144}\text{Nd}$ was determined using $^{146}\text{Nd}/^{144}\text{Nd}$ (0.7219) with an exponential fractionation law. The ^{149}Sm signal was used to correct the remaining ^{144}Sm interference on ^{144}Nd , using the $^{144}\text{Sm}/^{149}\text{Sm}$ ratio of 0.2301. The mass fractionation of $^{147}\text{Sm}/^{149}\text{Sm}$ was corrected by the $^{147}\text{Sm}/^{149}\text{Sm}$ normalization, using the interference-free $^{147}\text{Sm}/^{149}\text{Sm} = 1.08680$ and exponential law (Xu et al. 2015). The $\epsilon_{\text{Nd}}(t)$ values were calculated relative to the chondritic uniform reservoir (CHUR) parameters of Jacobsen and Wasserburg (1980) (present-day $^{143}\text{Nd}/^{144}\text{Nd} = 0.512638$ and $^{147}\text{Sm}/^{149}\text{Sm} = 0.1967$) with $^{143}\text{Nd}/^{144}\text{Nd}$ renormalized to $^{146}\text{Nd}/^{144}\text{Nd} = 0.7219$ (Hamilton et al. 1983; Bouvier et al. 2008).

In situ monazite U-Pb dating

In situ U-Pb dating of monazite was conducted using the same instruments and analytical methods described above for the titanite analyses. The spot size and frequency of the laser for U-Pb dating were set to 16 μm and 2 Hz. Monazite standard 44069 (Aleinikoff et al. 2006) and glass NIST610 were used as external standards for U-Pb dating and trace element calibration, respectively.

In situ trace element analyses of pyrite and magnetite

Trace element concentrations of pyrite and magnetite were analyzed by LA-ICP-MS. Detailed operating conditions and data reduction are similar to those described by Liu et al. (2008). An Agilent 7900 ICP-MS instrument equipped with a Geolas HD laser ablation system was used to acquire ion signal intensities. A "wire" signal smoothing device is included in the laser ablation system (Hu et al. 2015). For trace element analyses of pyrite, the spot size and frequency of the laser were set to 32 μm and 5 Hz, respectively. The sulfide reference material of MASS-1 (USGS) was used as an external bracketing standard. The data quality was monitored by analyzing the NIST 610 reference glass and the MASS-1 as unknowns interspersed with the measurements of the samples. For magnetite, the spot size and frequency of the laser were set to 44 μm and 5 Hz, respectively. Trace element compositions were calibrated against various reference materials (BHVO-2G, BCR-2G, and BIR-1G) without using an internal standard (Liu et al. 2008). Each analysis incorporated a background acquisition of approximately 20–30 s followed by 50 s of data acquisition. A Microsoft Excel-based spreadsheet ICP-MSDataCal was used in the identical fashion as indicated for trace element measurements above (Liu et al. 2008).

In situ S isotope analyses of pyrite and pyrrhotite

In situ sulfur isotope analyses of pyrite and pyrrhotite were performed on a Neptune Plus MC-ICP-MS equipped with a Geolas HD excimer ArF laser ablation system. Pyrite and pyrrhotite were both ablated using a large spot size (44 μm) and slow pulse frequency (2 Hz) to avoid the down-hole fractionation effect (Fu et al. 2016); 100 laser pulses were completed in one analysis. The laser fluence was kept constant at ~5 J/cm². The Neptune Plus was equipped with nine Faraday cups fitted with 10¹¹ Ω resistors. Isotopes ^{32}S , ^{33}S , and ^{34}S were collected in Faraday cups using static mode. A standard-sample bracketing method was employed to correct for instrumental mass fractionation. To avoid matrix effects, a pyrite standard PPP-1 (Gilbert et al. 2014) was chosen as a reference material for correcting the natural pyrite and pyrrhotite (Fu et al. 2016). In addition, the in-house reference pyrite SP-Py-01 ($\delta^{34}\text{S}_{\text{VCDT}} = 2.0 \pm 0.5\%$) and pyrrhotite SP-Po-01 ($\delta^{34}\text{S}_{\text{VCDT}} = 1.4 \pm 0.4\%$) were analyzed repeatedly as unknown samples to verify the accuracy of the calibration method. Standard errors for PPP-1, SP-Py-01, and SP-Po-01 are $\pm 0.2\%$ (2 σ ; N = 54), $\pm 0.2\%$ (2 σ ; N = 20), and $\pm 0.2\%$ (2 σ ; N = 4), respectively.

RESULTS

Textures and chemical compositions of titanite

Titanite crystals are ubiquitous in the biotite monzonite, showing a wide range of textures. These crystals are about 100–400 μm in length, euhedral to anhedral in shape. Three types of titanite

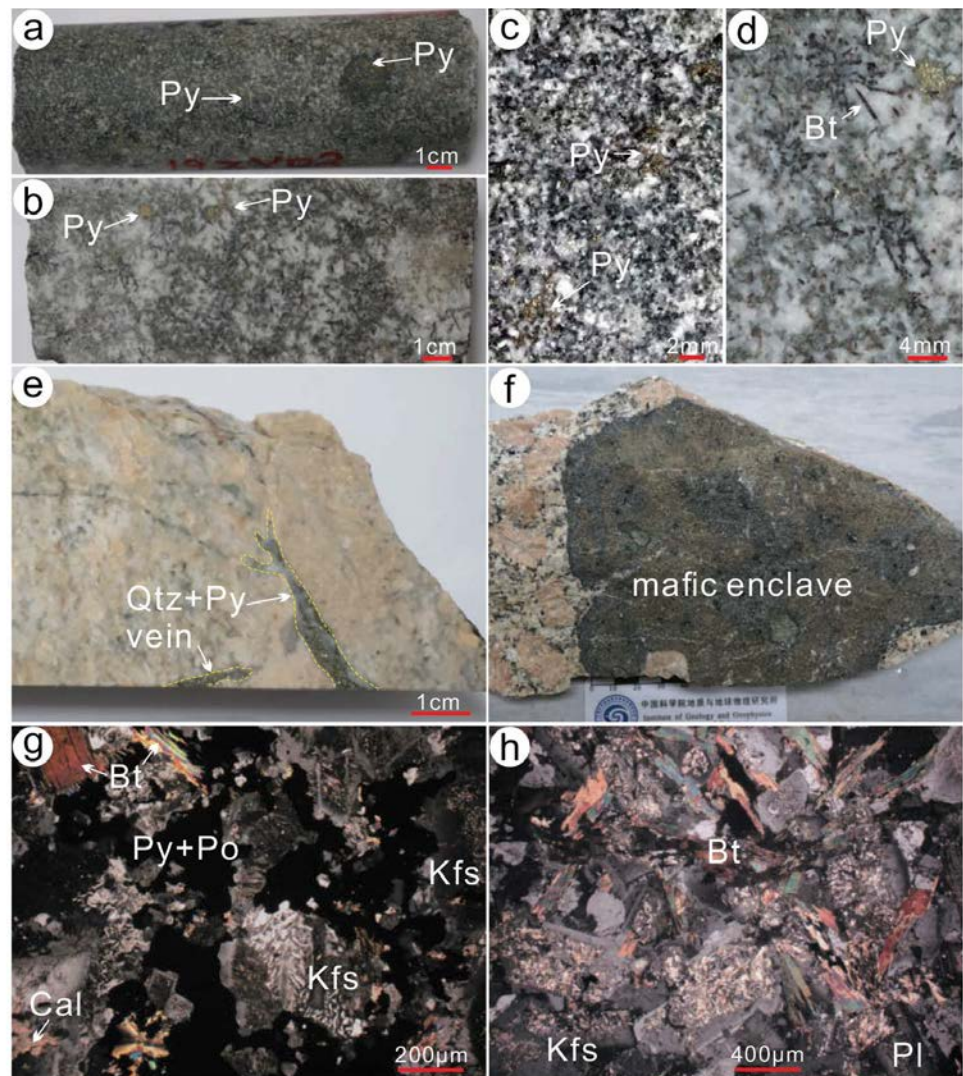
were identified based on their occurrence, petrographic features, and chemical compositions (Figs. 4 and 5; Online Materials¹ Fig. OM1). The titanite compositional data obtained are provided in Online Materials¹ Table OM1.

Type 1 titanite (Ttn1) typically displays discrete, euhedral-subhedral, and rhombus-shaped grains and occurs as intergrowths with plagioclase, K-feldspar, and biotite in the matrix. Oscillatory zoning is the most common and characteristic internal texture of Ttn1, consisting of alternating light and dark bands observed in BSE images (Figs. 4a and 4b). In some cases, Ttn1 also shows sector zoning consisting of patchy dark, light and/or oscillatory zones (Fig. 4a). These features suggest that Ttn1 is of magmatic origin. Ttn1 shows limited ranges of CaO (27.7–29.1 wt%), TiO₂ (34.6–37.9 wt%), and SiO₂ (30.2–31.8 wt%), and low contents of Al₂O₃ (0.94–2.23 wt%), FeO (0.59–1.57 wt%), and MnO (0.03–0.24 wt%) (Fig. 5). Trace element data show that Ttn1 has low concentrations of total REE (SREE = 862–9228 ppm, average 4431 ppm) and HFSE (Nb + Ta + Zr + Hf = 227–4964 ppm, average 1733 ppm), together with slight enrichment of Light REE over Heavy REE (LREE/HREE = 2.8–17.8, average 8.5), low-Lu/Hf ratios (0.1–0.6, aver-

age 0.3), and weakly negative Eu anomalies ($Eu_N/Eu_N^* = 0.5–0.9$, average 0.8) (Fig. 5; Online Materials¹ Fig. OM1). Ttn1 shows large variations in the contents of Pb (0.4–12.7 ppm, average 2.2 ppm), Th (1.8–398.8 ppm, average 94.0 ppm), U (0.3–518.2 ppm, average 57.6 ppm), and Y (60–2420 ppm).

Type 2 titanite (Ttn2) occurs as subhedral to anhedral crystals characterized by simple zoning comprising irregular bright cores and light-gray contrasting rims under BSE (Figs. 4c–4e). This type of titanite commonly shares planar contacts with pyrite. Ttn2 tends to have lower CaO (24.6–28.6 wt%), TiO₂ (31.1–37.1 wt%), and SiO₂ (28.4–30.8 wt%), but higher FeO (0.83–2.41 wt%) and MnO (0.13–0.33 wt%) relative to Ttn1 (Fig. 5). Ttn2 also shows significantly higher concentrations of REE (3221–37648 ppm, average 20766 ppm), HFSE (531–5040 ppm, average 2529 ppm), Y (633–4960 ppm, average 2643 ppm), Pb (0.7–12.9 ppm, average 5.6 ppm), Th (39.1–738.6 ppm, average 376.7 ppm), and U (4.8–291.5 ppm, average 86.0 ppm), but broadly similar enrichment of LREE over HREE with slightly higher ratios of LREE/HREE (11.7–30.3, average 21.4) and Lu/Hf (0.1–2.9, average 0.9) (Fig. 5; Online Materials¹ Fig. OM1). In addition, Ttn2 displays

FIGURE 3. Photographs of hand specimen and thin section cross-polarized illumination of biotite monzonite, containing disseminated pyrite. (a and c) Fresh-weakly altered biotite monzonite. (b and d) Silicified-sericitized biotite monzonite. (e) Quartz-pyrite veins in Luanjiahe granite. (f) Mafic enclave in Gushan granite. (g and h) Photomicrographs of biotite monzonite. Qtz = quartz; Kfs = K-feldspar; Pl = plagioclase; Bt = biotite; Cal = calcite; Py = pyrite. (Color online.)



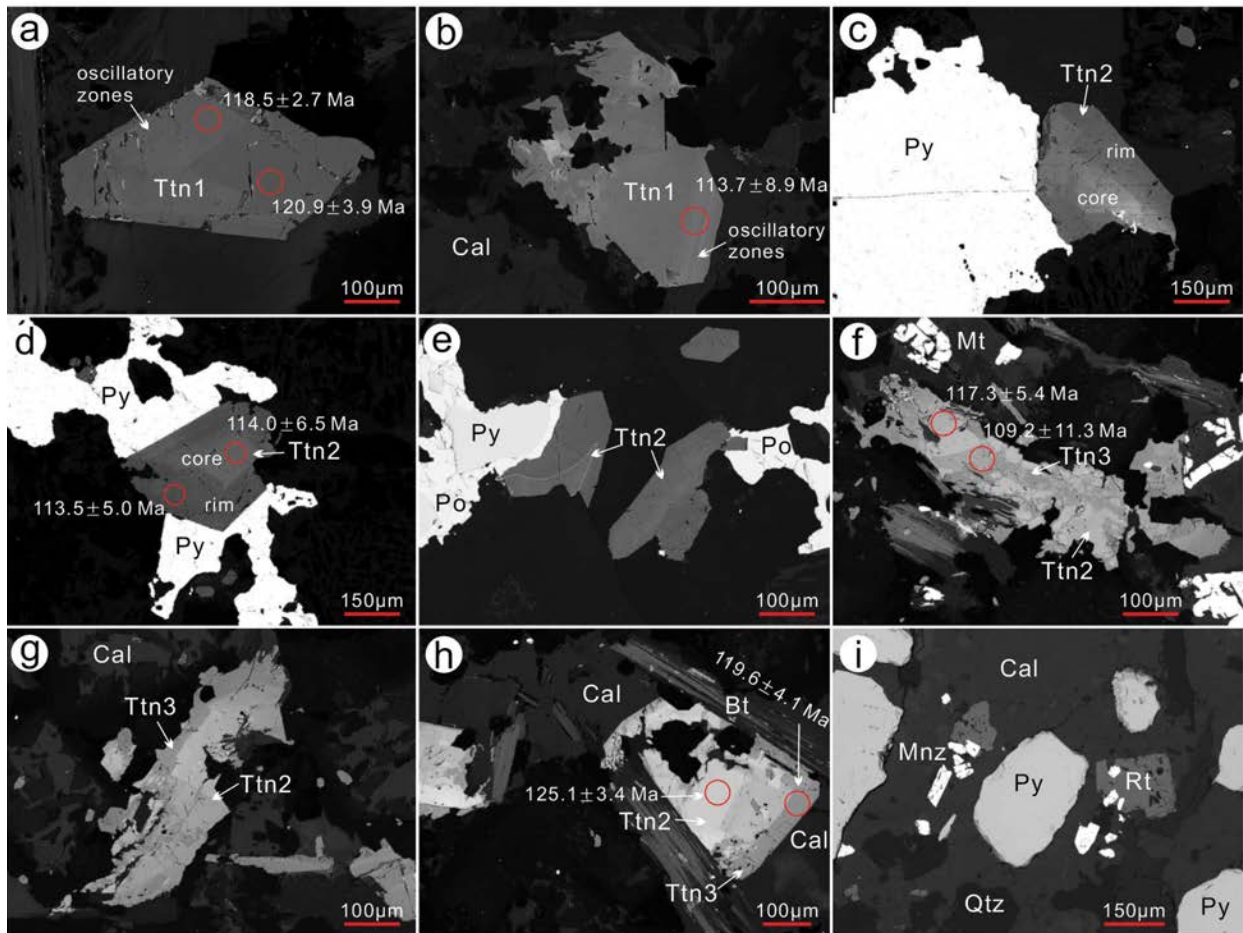


FIGURE 4. BSE images of three types of titanite and monazite. (a and b) Ttn1 with euhedral-subhedral shape and oscillatory zones. (c–e) Ttn2 with euhedral-subhedral shape and core-rim texture, coexisting with pyrite and pyrrhotite. (f–h) Dark-gray BSE Ttn3 penetrating and/or overgrowing Ttn2 and coexisting with calcite. (i) Hydrothermal monazite for U-Pb dating, from quartz-sulfide veins. Red circles show the location of points for LA-ICP-MS U-Pb dating, together with ^{207}Pb -corrected $^{206}\text{Pb}/^{238}\text{U}$ ages. Ttn = titanite; Py = pyrite; Po = pyrrhotite; Mt = magnetite; Cal = calcite; Bt = biotite; Qtz = quartz; Mnz = monazite; Rt = rutile. (Color online.)

more prominent negative Eu anomalies ($\text{Eu}_N/\text{Eu}_N^* = 0.3\text{--}0.7$, average 0.50) than Ttn1.

Type 3 titanite (Ttn3) occurs as fine, irregular veins penetrating and overgrowing Ttn2 (Figs. 4f–4h). Ttn3 commonly occurs together with calcite and displays dark gray color under BSE. Ttn3 has similar ranges of CaO (27.3–28.9 wt%), TiO_2 (34.7–37.8 wt%), SiO_2 (30.3–31.3 wt%), and Al_2O_3 (0.98–2.05 wt%) to Ttn1, but slightly higher contents of FeO (0.67–2.23 wt%) and MnO (0.05–0.23 wt%) (Fig. 5). The contents of trace elements of Ttn3 lie mostly between those of Ttn1 and Ttn2, with REE (SREE = 1173–28457 ppm, average 10144 ppm), HFSE (123–8136 ppm, average 2344 ppm), Pb (0.5–6.8 ppm, average 2.8 ppm), Th (14.8–511.2 ppm, average 157.4 ppm), U (1.7–197.0 ppm, average 36.3 ppm), and Y (197–5389 ppm, average 2049 ppm). Ttn3 also displays moderate Lu/Hf ratios (0.2–1.5, average 0.5), and a slight enrichment of LREE relative to HREE (LREE/HREE = 6.2–18.6, average 13.0), showing flat chondrite-normalized REE patterns with negative Eu anomalies ($\text{Eu}_N/\text{Eu}_N^* = 0.2\text{--}1.1$, average 0.6), similar to that of Ttn1 and Ttn2 (Online Materials¹ Fig. OM1).

Geochronology of the biotite monzonite and hydrothermal event

Titanite U-Pb ages. In situ titanite U-Pb isotopic data are listed in Table 1. Locations of representative points for U-Pb dating are shown in Figure 4. The uncorrected data were plotted on Tera-Wasserburg Concordia diagrams (Figs. 6a and 6b), and a regression through these data yielded a lower-intercept age. The y-intercept represents the initial $^{207}\text{Pb}/^{206}\text{Pb}$ ratio, which can be used to conduct ^{207}Pb -correction to calculate the corrected $^{206}\text{Pb}/^{238}\text{U}$ age (Aleinikoff et al. 2002). The magmatic titanites (Ttn1) define a lower-intercept age of 120.7 ± 3.1 Ma (2s, $n = 18$, MSWD = 1.8) with initial $^{207}\text{Pb}/^{206}\text{Pb} = 0.8516$. With this common Pb composition, a ^{207}Pb -correction was conducted. Ten points yield a weighted average $^{206}\text{Pb}/^{238}\text{U}$ age of 118.8 ± 2.2 Ma (MSWD = 1.3) (Fig. 6a), consistent within error with the lower-intercept age. However, eight points exhibit lower U and Pb with higher percentage of common Pb, plotting away from the lower intercept and resulting in greater experimental errors. They cannot yield convincing $^{206}\text{Pb}/^{238}\text{U}$ ages based on ^{207}Pb -correction, thus

the lower-intercept age (120.7 ± 3.1 Ma) is used as the magmatic titanite age. The hydrothermal titanites (Ttn2 and Ttn3) give a lower-intercept age of 120.9 ± 2.6 Ma ($2s$, $n = 19$, $MSWD = 1.4$) with initial $^{207}\text{Pb}/^{206}\text{Pb} = 0.8530$. Fifteen points define a ^{207}Pb -corrected weighted average $^{206}\text{Pb}/^{238}\text{U}$ age of 117.9 ± 2.2 Ma ($MSWD = 1.1$), which is consistent with the lower-intercept age (Fig. 6b). The other four points, plotting away from the lower intercept, failed to produce convincing $^{206}\text{Pb}/^{238}\text{U}$ ages, thus the lower-intercept age (120.9 ± 2.6 Ma) is used as the hydrothermal titanite age. It is noteworthy that the $^{206}\text{Pb}/^{238}\text{U}$ ages for Ttn2 and Ttn3, as well as cores and rims in Ttn2, are indistinguishable, thus they were regarded as a whole during age analysis.

Monazite U-Pb ages. The in situ U-Pb data of 19 spots on monazite grains are presented in Table 1. All the analyzed monazite grains are associated or intergrown with pyrite in the quartz-pyrite veinlets (Fig. 4i), thus their crystallization ages represent the timing of the hydrothermal (vein-forming) event. The U-Pb data give a lower-intercept age of 119.0 ± 5.8 Ma ($2s$, $n = 19$, $MSWD = 1.1$) on the Tera-Wasserburg Concordia diagram. The initial $^{207}\text{Pb}/^{206}\text{Pb}$ value is 0.7373. The ^{207}Pb -corrected weighted average $^{206}\text{Pb}/^{238}\text{U}$ age is 118.2 ± 4.6 Ma ($MSWD = 0.2$), which is consistent with the lower intercept age (Fig. 6c).

Nd isotopic composition of titanite

In situ Nd isotopic compositions of titanite are shown in Online Materials¹ Table OM1. The analyzed Ttn1, Ttn2, and Ttn3 show restricted and indistinguishable $\epsilon_{\text{Nd}}(t = 121 \text{ Ma})$ values of -14.7 to -13.0 , -14.7 to -13.5 , and -14.3 to -12.9 (Fig. 7).

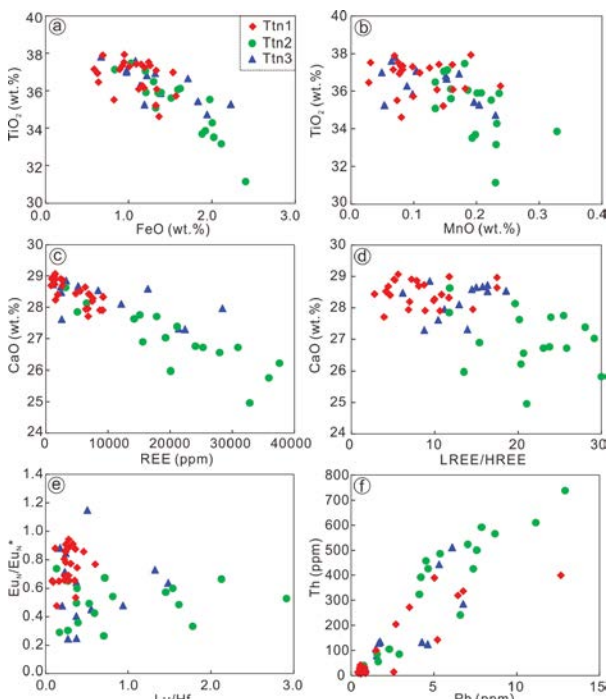


FIGURE 5. Selected binary plots showing the geochemical characteristics of three types of titanite. Plots of (a) TiO_2 vs. FeO , (b) TiO_2 vs. MnO , (c) CaO vs. REE, (d) CaO vs. LREE/HREE, (e) $^*\text{Eu}_N/\text{Eu}_N$ vs. Lu/Hf , (f) Th vs. Pb . (Color online.)

Classification, trace-element, and sulfur isotopic compositions of pyrite, magnetite, and pyrrhotite

Based on occurrence, optical characteristics, and mineral assemblages, four types of pyrite were recognized. The complete data set of trace element concentrations and sulfur isotopes are given in Online Materials¹ Table OM2.

Type 1 pyrite (Py1) occurs in the fresh biotite monzonite. It is characterized by isolated euhedral-anhedral crystals coexisting with magnetite and contains inclusions of plagioclase, quartz, and

TABLE 1. Results of in-situ LA-ICP-MS U-Pb dating on titanite and monazite

Spot no.	Isotopic ratios						^{207}Pb -Corr. Age (Ma)		
	$^{207}\text{Pb}/^{206}\text{Pb}$	1σ	$^{207}\text{Pb}/^{235}\text{U}$	1σ	$^{206}\text{Pb}/^{238}\text{U}$	1σ	Rho	$^{206}\text{Pb}/^{238}\text{U}$	1σ
Magmatic Ttn1									
1	0.1598	0.0208	0.3634	0.0221	0.0211	0.0008	0.61	116.1	4.9
2	0.2606	0.0235	0.6647	0.0403	0.0234	0.0009	0.65	110.1	5.8
3	0.1633	0.0274	0.6964	0.0738	0.0234	0.0019	0.75	128.3	11.8
4	0.0729	0.0044	0.1717	0.0086	0.0182	0.0005	0.50	112.7	2.9
5	0.2633	0.0319	0.6636	0.0451	0.0243	0.0014	0.86	113.7	8.9
6	0.0766	0.0048	0.1939	0.0102	0.0192	0.0004	0.42	118.5	2.7
7	0.1197	0.0086	0.3036	0.0164	0.0208	0.0006	0.54	120.9	3.9
8	0.0627	0.0024	0.1663	0.0058	0.0195	0.0003	0.44	122.4	1.9
9	0.0921	0.0056	0.2367	0.0107	0.0197	0.0004	0.47	119.1	2.7
10	0.2415	0.0223	0.7310	0.0459	0.0243	0.0012	0.77	117.7	7.4
11	0.1194	0.0243	1.1518	0.1443	0.0287	0.0027	0.76	166.9	17.1
12	0.0866	0.0265	7.4754	1.3708	0.0813	0.0131	0.88	485.7	78.0
13	0.4009	0.0605	33.8111	3.6589	0.2907	0.0282	0.89	1002.1	140.6
14	0.2696	0.0315	6.4758	0.4805	0.0707	0.0051	0.98	323.7	30.9
15	0.2094	0.0407	4.5784	0.6724	0.0599	0.0062	0.70	303.0	37.5
16	0.2757	0.0431	16.8791	1.9652	0.1484	0.0133	0.77	662.4	74.4
17	0.1520	0.0297	2.6638	0.2484	0.0382	0.0033	0.92	211.3	20.4
18	0.3438	0.0383	4.1160	0.2788	0.0578	0.0037	0.95	232.0	22.6
Hydrothermal Ttn2 and Ttn3									
1	0.2123	0.0221	0.4920	0.0286	0.0224	0.0010	0.79	114.0	6.5
2	0.2795	0.0168	0.8772	0.0412	0.0249	0.0008	0.68	113.5	5.0
3	0.1340	0.0066	0.3677	0.0143	0.0208	0.0005	0.58	118.8	2.9
4	0.1493	0.0062	0.4139	0.0138	0.0208	0.0004	0.60	116.1	2.6
5	0.3672	0.0403	1.6644	0.1172	0.0315	0.0019	0.86	121.6	12.0
6	0.3558	0.0225	1.1918	0.0577	0.0279	0.0012	0.86	110.0	7.3
7	0.4104	0.0244	1.7262	0.0935	0.0328	0.0011	0.60	115.3	6.7
8	0.1584	0.0059	0.4712	0.0157	0.0220	0.0005	0.66	121.2	3.0
9	0.2281	0.0108	0.7052	0.0224	0.0243	0.0006	0.80	120.7	3.9
10	0.2814	0.0174	0.9036	0.0474	0.0259	0.0009	0.63	117.3	5.4
11	0.4367	0.0301	1.9547	0.1623	0.0330	0.0018	0.66	109.2	11.3
12	0.4134	0.0277	1.5193	0.0632	0.0318	0.0012	0.91	111.0	7.5
13	0.1636	0.0086	0.4884	0.0188	0.0229	0.0005	0.61	125.1	3.4
14	0.2364	0.0104	0.7566	0.0281	0.0244	0.0007	0.72	119.6	4.1
15	0.2455	0.0192	0.6450	0.0320	0.0222	0.0008	0.69	107.2	4.8
16	0.4707	0.0257	1.9566	0.0717	0.0333	0.0010	0.86	101.1	6.5
17	0.4220	0.0347	1.2847	0.0570	0.0290	0.0012	0.89	99.4	7.2
18	0.4063	0.0502	3.0899	0.2263	0.0416	0.0026	0.86	147.4	16.2
19	0.6842	0.0661	3.9290	0.1787	0.0524	0.0024	0.99	70.4	14.5
Hydrothermal monazite									
1	0.1665	0.0250	0.4325	0.0443	0.0216	0.0012	0.55	117.3	7.6
2	0.1043	0.0149	0.2680	0.0294	0.0203	0.0007	0.30	120.6	4.2
3	0.5016	0.0710	2.0192	0.2391	0.0380	0.0033	0.73	102.8	20.4
4	0.4416	0.0742	1.9995	0.2439	0.0360	0.0026	0.60	114.9	16.4
5	0.6665	0.0535	6.8691	0.4026	0.0806	0.0038	0.81	110.1	22.8
6	0.5684	0.0582	3.6402	0.3118	0.0542	0.0030	0.65	117.1	18.4
7	0.5088	0.0335	3.0583	0.1813	0.0454	0.0019	0.72	120.0	12.0
8	0.2305	0.0216	0.7186	0.0597	0.0241	0.0011	0.56	118.1	7.0
9	0.6125	0.0599	3.9060	0.2581	0.0598	0.0029	0.73	107.9	17.5
10	0.2241	0.0256	0.8614	0.1738	0.0234	0.0020	0.42	116.0	12.6
11	0.4499	0.0262	2.3441	0.1800	0.0387	0.0018	0.62	120.9	11.4
12	0.4165	0.0691	1.7802	0.4106	0.0365	0.0039	0.47	124.1	24.4
13	0.2326	0.0330	0.8270	0.1462	0.0261	0.0016	0.35	127.4	10.0
14	0.2546	0.0323	0.8865	0.1923	0.0253	0.0020	0.36	119.0	12.5
15	0.2728	0.0438	0.7743	0.0685	0.0248	0.0011	0.50	113.4	6.9
16	0.3956	0.0681	1.5283	0.1612	0.0322	0.0021	0.62	114.9	13.1
17	0.2882	0.0314	1.1070	0.1890	0.0273	0.0021	0.45	121.1	13.0
18	0.5109	0.0831	2.0165	0.2047	0.0396	0.0032	0.79	104.3	19.8
19	0.6057	0.1017	3.6096	0.3799	0.0574	0.0056	0.92	106.8	33.9

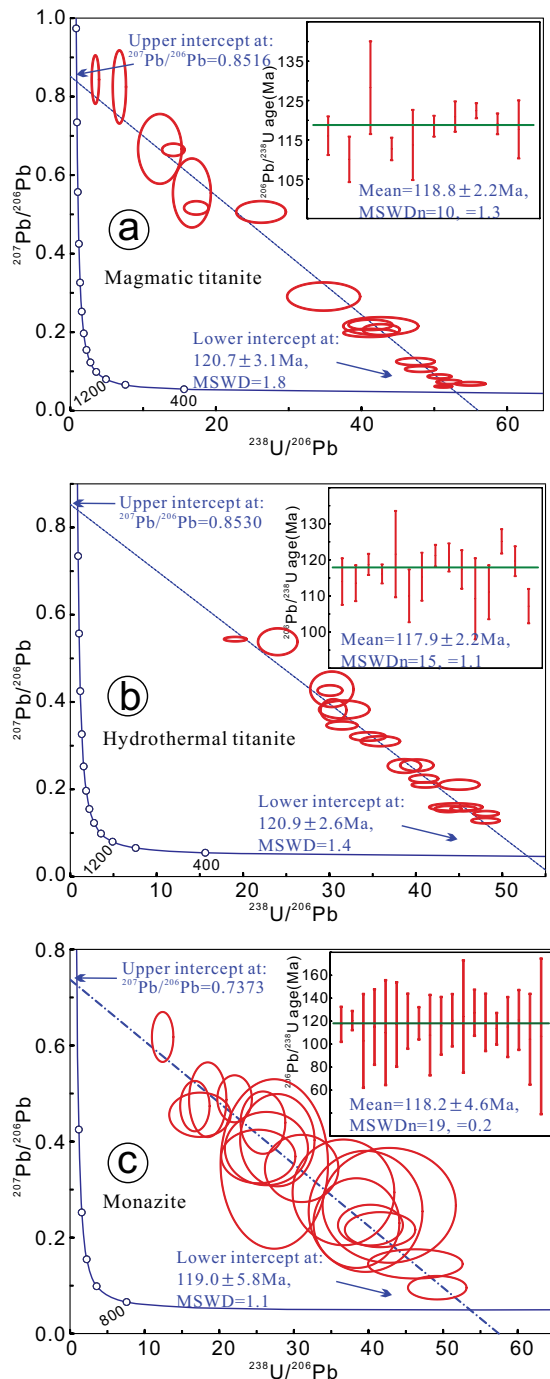


FIGURE 6. Tera-Wasserburg diagrams and corresponding weighted mean plots of age data for (a) magmatic titanite (Ttn1), (b) hydrothermal titanite (Ttn2, Ttn3) from the biotite monzonite, and (c) hydrothermal monazite from the quartz-pyrite veins. (Color online.)

titanite (Figs. 8a and 8e). The Py1 contains uniformly low concentrations of Co (3–374 ppm), Ni (3–41 ppm), Cu (0–7.9 ppm), Zn (0–4.1 ppm), As (0.2–0.9 ppm), Ag (0–0.05 ppm), Sb (0–0.09 ppm), Au (0–0.03 ppm, with two outliers at 0.1 and 0.14 ppm), Pb (0–8.5 ppm), and Bi (0–6.1 ppm) (Fig. 9). It

commonly displays homogeneous textures on BSE images (Fig. 8e), contrasting with heterogeneous compositional textures of Py2 and Py3 (Figs. 8f and 8g). The $\delta^{34}\text{S}$ values of Py1 are relatively low with a large variation from +1.9 to +6.3‰ (average +4.7‰) (Fig. 10). The coexisting magnetite grains mostly plot within the magmatic magnetite region on the Ti vs. Ni/Cr diagram (Dare et al. 2014) with low Ni/Cr ratios (0.02–0.93) (Online Materials! Fig. OM2).

Type 2 pyrite (Py2) mostly occurs as anhedral clusters in the altered monzonite, which shows significant sericitization and carbonation. The Py2 is commonly enclosed within and cross-cut by pyrrhotite (Figs. 8b and 8f), suggesting that Py2 formed earlier than pyrrhotite. It is likely partly replaced by pyrrhotite, resulting in corroded grain boundaries and metasomatic-relict texture (Fig. 8b). Trace element data show that the contents of Co (0.1–4837 ppm), Ni (0–87.6 ppm), As (0.3–86.4 ppm), Ag (0–0.4 ppm), Sb (0–4.5 ppm), Au (0–0.09 ppm, with one outlier of 18.7 ppm), Pb (0–218 ppm) and Bi (0–9.9 ppm, with an outlier of 16.8 ppm) in Py2 have large variations and are higher than Py1 (Fig. 9). The $\delta^{34}\text{S}$ values of Py2 are +6.4 to +9.5‰ (average +8.4‰) (Fig. 10), which are higher than Py1 but similar to the $\delta^{34}\text{S}$ values of pyrite from other deposits in the Jiaodong Au province (+6 to +10‰; Mao et al. 2008; Feng et al. 2018; Li et al. 2018; Deng et al. 2020b). The pyrrhotite has a $\delta^{34}\text{S}$ range of +6.9 to +8.8‰ (average +7.9‰) that overlaps with the range of Py2.

Type 3 pyrite (Py3) occurs as subhedral, rounded crystals in the quartz-pyrite veins (Figs. 8c and 8g). The Py3 contains low concentrations of Co (0–98.6 ppm), Ni (0–116 ppm), Cu (0–0.5 ppm), Zn (0.4–0.9 ppm), Ag (0–0.3 ppm), Sb (0–0.1 ppm), Au (0–0.01 ppm, with an outlier of 0.1 ppm), Pb (0–2.2 ppm) and Bi (0–1.0 ppm, with an outlier of 19.9 ppm), but markedly high contents of As (325–852 ppm) (Fig. 9). The $\delta^{34}\text{S}$ values of Py3 are +6.5 to +7.6‰ (average +7.2‰), which is entirely within the range of Py2 (Fig. 10).

Another type of pyrite (Py4) was sampled from the mafic enclaves of the Gushan granite. It occurs as euhedral to anhedral

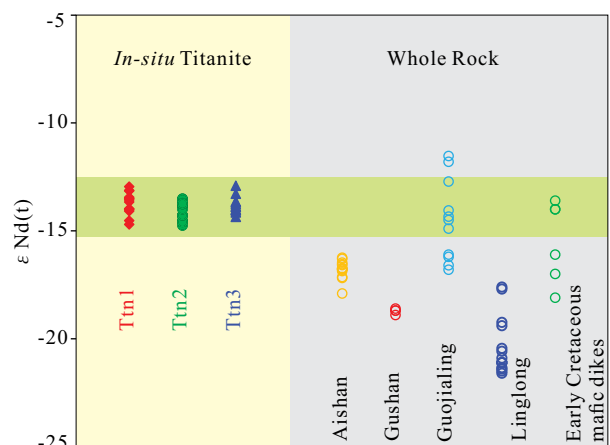


FIGURE 7. $\epsilon_{\text{Nd}}(t)$ values of titanite from biotite monzonite, and comparison with whole-rock $\epsilon_{\text{Nd}}(t)$ values of Mesozoic magmatic rocks in the Jiaodong Peninsula. Data are from Li et al. (2012b); Yang et al. (2012); Cai et al. (2013); Li et al. (2019a); and this study. (Color online.)

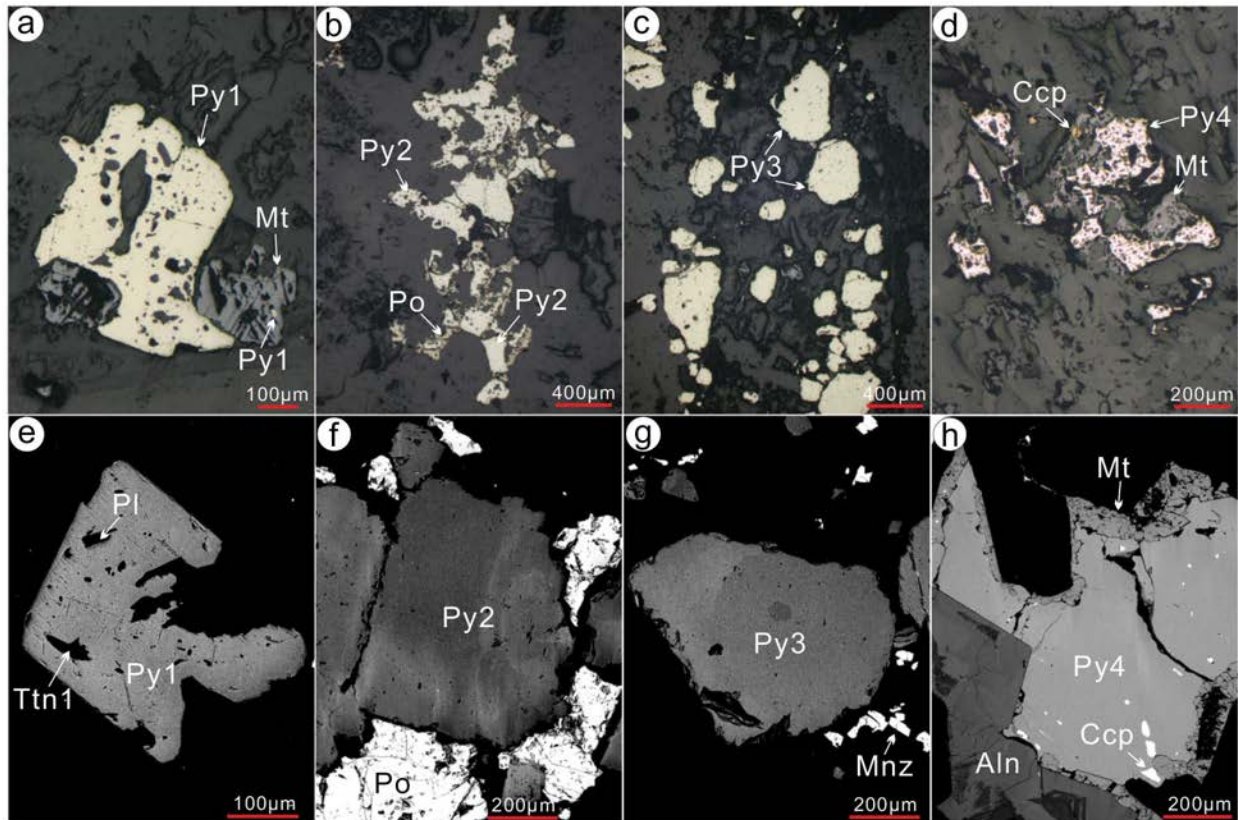


FIGURE 8. Reflected light photomicrographs and BSE images of four types of pyrite. (a and e) Py1 with homogeneous texture under BSE is from the fresh to weakly altered biotite monzonite, coexisting with magnetite, enclosing magmatic titanite and plagioclase. (b and f) Py2 occurs with pyrrhotite and shows heterogeneous texture under BSE, from silicified-sericitized biotite monzonite. (c, g) Py3 is from the quartz-pyrite veins, showing systematic zones. (d and h) Py4 is from the mafic enclave in the Gushan granite, occurring with magnetite, chalcopyrite, and allanite. Py = pyrite; Po = pyrrhotite; Mt = magnetite; Ccp = chalcopyrite; Ttn = titanite; Pl = plagioclase; Mnz = monazite; Aln = allanite. (Color online.)

crystals in the matrix and commonly coexists with magnetite and minor chalcopyrite (Figs. 8d and 8h). Most of the trace elements, including Co, Cu, Zn, As, Sb, Au, Pb, and Bi, show low concentrations (mostly below detection limits), but the contents Ag (0–2.85 ppm) and Ni (227–3407 ppm) are relatively high and vary widely. The Py4 displays a low and narrow range of $\delta^{34}\text{S}$ values from +5.0 to +6.4‰ (average +5.9‰) (Fig. 10).

DISCUSSION

Origins of the different generations of titanite

Distinct origins of titanite can be discriminated by their textures, paragenetic mineral assemblages, and chemical compositions (Cao et al. 2015; Fu et al. 2016). The Ttn1 grains are mostly euhedral and rhombus-shaped, show oscillatory and sector zoning under BSE, and occur as intergrowths with igneous plagioclase, K-feldspar, and biotite in the matrix of the biotite monzonite, implying a magmatic origin. In contrast, the Ttn2 and Ttn3 grains are mostly subhedral to anhedral, show core-rim texture and penetrating relationship under BSE, and commonly show planar contacts with hydrothermal pyrite, sericite, and calcite, suggesting a hydrothermal origin. This conclusion is further supported by the chemical compositions of the titanite grains. As demonstrated in Figure 5, Ttn1 shows low Fe, Mn,

REE, and high Ti, Ca. The Ttn1 data fall in relatively restricted portions of these four diagrams, resembling typical magmatic titanite. In contrast, Ttn2 and Ttn3 are much more compositionally diverse, with relatively higher Fe, Mn, REE, and lower Ti, Ca contents: all characteristics of hydrothermal titanite (Morad et al. 2009; Fu et al. 2016). The high Fe and Mn contents of Ttn2 and Ttn3 are consistent with Fe-rich hydrothermal fluids from which pyrite and pyrrhotite formed. Overall, Figures 5a and 5c show negative correlations between TiO_2 and FeO, CaO and REE, respectively, indicating that appreciable amounts of Fe and REE substitute for Ti and Ca in the titanite structure, which is common in hydrothermal titanite (Cao et al. 2015; Li et al. 2021). The dominant substitution mechanisms are likely to be: $(\text{Al,Fe})^{3+} + (\text{F,OH})^- = \text{Ti}^{4+} + \text{O}^{2-}$, in which the substitution of Fe for Ti predominates, and $\text{REE}^{3+} + (\text{Al,Fe})^{3+} = \text{Ca}^{2+} + \text{Ti}^{4+}$ (Olin and Wolff 2012; Xie et al. 2010).

Our results indicate that the concentrations of trace elements, including REE, HFSE, Th, U, and Pb, are quite distinct between magmatic (Ttn1) and hydrothermal (Ttn2 and Ttn3) titanites (Fig. 5). These differences in trace elements are strongly affected by the formation conditions, such as T , f_{O_2} , f_{S_2} , and composition of melt or fluid (Tiepolo et al. 2002; Cao et al. 2015; Xiao et al. 2021). Hydrothermal Ttn2 and Ttn3 show higher HFSE

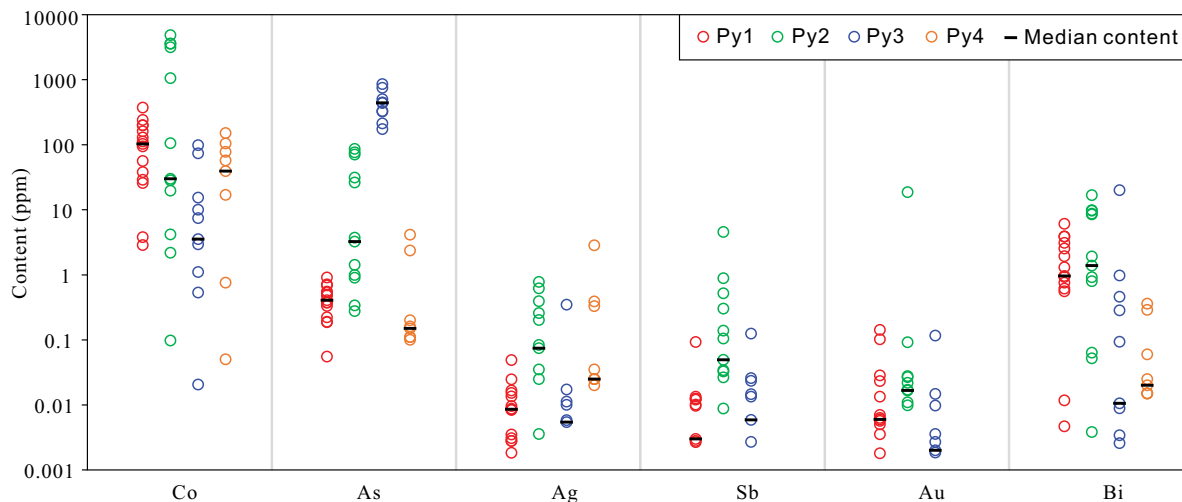


FIGURE 9. Trace elements of four types of pyrite. Note that some data with a value of 0 are not plotted on the diagram, and the contents of Sb and Au for Py4 are below the detection limit. (Color online.)

concentrations and Lu/Hf ratios than the magmatic Ttn1, similar to hydrothermal titanites from other regions documented by Fu et al. (2016) and Xiao et al. (2021). Enrichment of HFSE in hydrothermal titanite suggests that HFSE can be mobile in hydrothermal fluids during silicification, sericitization, and carbonation. However, in contrast to other studies, the hydrothermal titanites (Ttn2 and Ttn3) have higher Σ REE compared with magmatic titanite (Ttn1). This implies that the hydrothermal fluids were relatively enriched in REE. This interpretation is also consistent with the ubiquitous presence of monazite in the quartz-pyrite veins.

Despite the differences in REE contents, the magmatic and hydrothermal titanites show similar chondrite-normalized REE patterns (Online Materials¹ Fig. OM1), which suggest that the hydrothermal fluids that precipitated Ttn2 and Ttn3 were most likely exsolved from the same monzonitic magma that crystallized Ttn1. This conclusion is further supported by the overlapping crystallization ages of magmatic Ttn1 (120.7 ± 3.1 Ma)

and hydrothermal Ttn2 and Ttn3 (120.9 ± 2.6 Ma), and by the indistinguishable $\epsilon_{Nd}(t)$ values of the three titanite types (Fig. 7). The latter also implies the same Nd isotope composition of the monzonitic magma and hydrothermal fluids, further suggesting the co-genetic origin between magma and fluid.

Given its high Nd content, magmatic titanite could shed light on the Nd isotope composition of the magma (e.g., Xie et al. 2010; Cao et al. 2015). The homogeneous $\epsilon_{Nd}(t)$ values (-14.7 to -13.0) of magmatic Ttn1 are higher than the whole-rock $\epsilon_{Nd}(t)$ values of the lower crustal-sourced Linglong granite (-21.6 to -19.2), Gushan granite (-18.9 to -18.6), and Aishan granite (-17.9 to -16.2) (Yang et al. 2012; Li et al. 2012b, 2019a), but within the range of the Guojialing granodiorite (-16.8 to -11.5), which has been interpreted as deriving from a mixture of mantle and lower crustal sources (Yang et al. 2012; Li et al. 2019a). Additionally, early Cretaceous mafic dikes in the Jiaodong area have $\epsilon_{Nd}(t)$ that overlap with the range of Ttn1 (-18.1 to -13.6 ; Cai et al. 2013) (Fig. 7). Taken as a whole, these data support a mixed mantle and lower crustal source for the monzonitic magma (Fig. 11a).

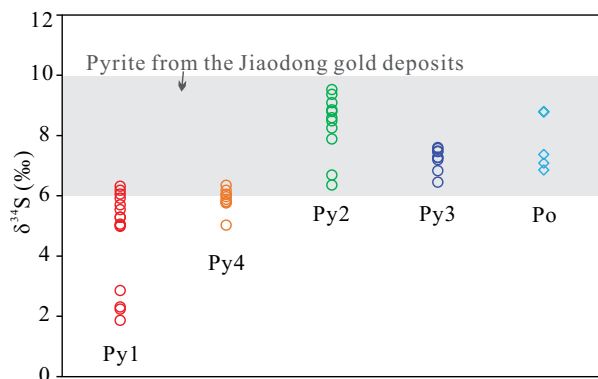


FIGURE 10. In situ sulfur isotopes of four types of pyrite and pyrrhotite. The $\delta^{34}S$ peak of pyrite from the Jiaodong Au province is from Mao et al. (2008), Feng et al. (2018), Li et al. (2018), and Deng et al. (2020b). (Color online.)

Interpretation of pyrite geochemistry

Trace elements and S isotopes of pyrite record valuable information about the source and properties (pH, redox, temperature) of the fluids from which the pyrite formed (Pokrovski et al. 2002; Deditius et al. 2014; Peterson and Mavrogenes 2014; Li et al. 2018). Four types of pyrite identified in this study have been characterized for trace elements and S isotopes, and the implications of these results are discussed here.

The isolated Py1 grains show features consistent with a magmatic origin, including disseminated occurrence in fresh monzonite; coexistence with magmatic magnetite, plagioclase, quartz, and titanite; homogeneous BSE response; and low concentrations of trace metals (Co, Ni, Cu, Zn, As, Ag, Sb, Pb, and Bi). The Py1 grains also show several similarities with Py4 grains found in the fresh mafic enclaves from the Gushan granite. The Py4 occurs as euhedral to anhedral crystals in the matrix and

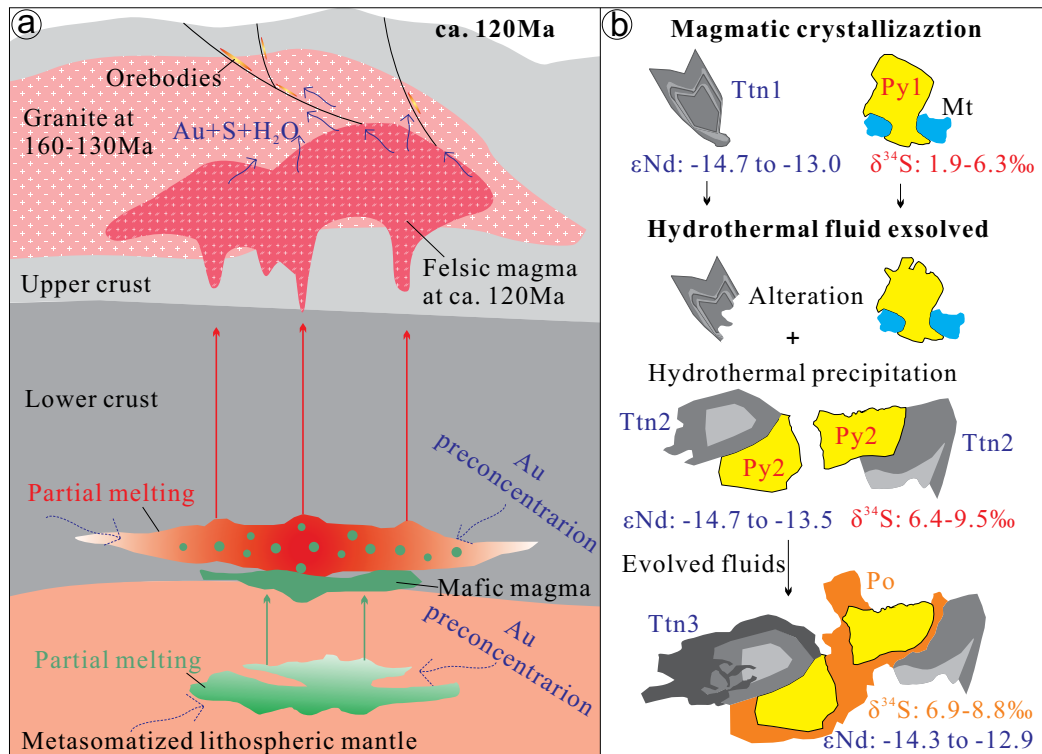


FIGURE 11. Schematic diagram showing (a) the formation of biotite monzonite, and the contribution of magmatic-hydrothermal fluids to Au deposits in the Jiaobei Terrane; (b) titanite and pyrite fingerprint of hydrothermal fluids exsolved from the monzonitic magma. The monzonite formed by partial melting of the lower crust of the NCC with involvement of mantle materials at ca. 120 Ma, probably leading to preconcentration of Au, releasing auriferous magmatic-hydrothermal fluids at late stage. (Color online.)

coexists with magnetite and allanite (Figs. 8d and 8h). Both Py1 and Py4 are therefore interpreted as being of magmatic origin. Both Py1 and Py4 also have broadly similar and relatively low values of $\delta^{34}\text{S}$ (+1.9 to +6.3‰ and +5.0 to +6.4‰, respectively), which represent the sulfur isotopic compositions of the magma. Previous research has suggested that the mafic enclaves from the Gushan granite were formed by mixing mafic with felsic magmas (Li et al. 2012b), during which both chemical and isotopic compositions tend to reach homogenization. The felsic magma was sourced from the ancient NCC lower crust at ca. 120 Ma, and the mafic magma was derived from an enriched lithospheric mantle source beneath eastern NCC (Li et al. 2012b). Similarly, the above results of Nd isotopes in titanite suggest a potentially mixed mantle/lower crustal source for the monzonitic magma at ca. 121 Ma. Thus, we interpret that the sulfur isotopic compositions of Py1 and Py4 represent the products of isotopic exchange between lower crust-derived felsic magma and lithospheric mantle-derived mafic magma.

In contrast to Py1 and Py4, Py2 and Py3 show features typical of hydrothermal origin. Py2 occurs mostly as anhedral clusters in the altered monzonite, coexists with sericite, calcite, and pyrrhotite, and displays heterogeneous textures (Fig. 8f). In addition, Py2 shows variable and relatively high concentrations of minor and trace metals (especially Co, As, Ag, Sb, and Bi). Significantly, extremely high contents of Au (18.7 ppm) and Bi (16.8 ppm) suggest the presence of gold as submicrometer inclu-

sions in Py2. The latter implies that the hydrothermal fluids that deposited Py2 had the potential for precious metal mineralization. Py3 occurs in the quartz-pyrite veins and thus is unambiguously of hydrothermal origin. Py3 shows various broad similarities with pyrite from the Jiaodong Au province, especially high-As contents and $\delta^{34}\text{S}$ values of +6.5 to +7.6‰.

Pyrrhotite grains commonly occur as rims on or fracture fill within the Py2 grains, implying that pyrrhotite formed later than Py2. However, the pyrrhotite and Py2 display similar $\delta^{34}\text{S}$ values ($\delta^{34}\text{S}_{\text{po}} = +6.9$ to +8.8‰, $\delta^{34}\text{S}_{\text{Py2}} = +6.4$ to +9.5‰), which are indicative of natural sulfur isotopic fractionation between pyrite and pyrrhotite precipitated from hydrothermal fluids with the same sulfur ratios ($\delta^{34}\text{S}$) (e.g., Li et al. 2017). The precipitation of early pyrite transitioning to later pyrrhotite suggests a decrease of sulfur fugacity in the evolving hydrothermal fluid, probably due to the consumption of sulfur by pyrite or perhaps by the effervescence of H_2S .

Considering that the hydrothermal sulfides disseminated in the monzonite are dominated by pyrite and pyrrhotite, isotopic fractionation between sulfide pairs is negligible, thus the sulfur isotopic signature of pyrite can reasonably represent the bulk sulfur isotopic composition of the hydrothermal fluid (Ohmoto 1972). Sulfur isotopes of pyrite have been widely used to trace the sources of fluids (e.g., Peterson and Mavrogenes 2014; Chen et al. 2015). Based on the sulfur isotopic ratios of Py2 and Py3, we suggest that the corresponding hydrothermal fluids have a narrow

range of $\delta^{34}\text{S}$ values (+6.4 to +9.5‰), similar to those from the Au deposits in the Jiaodong province (+6 to +10‰; Li et al. 2018; Feng et al. 2018; Deng et al. 2020b), but are slightly heavier than the monzonitic magma represented by the $\delta^{34}\text{S}$ of Py1 (+1.9 to +6.3‰) (Fig. 10). The textural, geochemical, and geochronological observations of the magmatic-hydrothermal titanite indicate a role of magmatic-hydrothermal fluids that exsolved from the monzonitic magma. These magmatic-hydrothermal fluids are likely to have contributed to the precipitation of Py2 and Py3, as well as to silicification, sericitization, and carbonation of the biotite monzonite. Experimental data from Fiege et al. (2014) revealed that the hydrothermal fluids released by magma degassing could have heavier S isotopes than the source magma (with $\delta^{34}\text{S}$ ~6.7‰ higher) when the sulfur occurs as S^{2-} or H_2S . This is compatible with the slightly heavier $\delta^{34}\text{S}$ values of the hydrothermal Py2 and Py3 compared to the magmatic Py1. In addition, the age of hydrothermal monazite (118.2 ± 4.6 Ma) is consistent with that of biotite monzonite (120.7 ± 3.1 Ma), further implying an intimate relationship between the monzonitic magma and hydrothermal fluids. In general, we propose that the hydrothermal fluids that precipitated Py2 and Py3 were directly exsolved from the monzonitic magma, which had previously crystallized igneous Py1 grains.

Constraints on magmatism and hydrothermal processes

The deposition of titanite and pyrite in the biotite monzonite clearly spans the magmatic and hydrothermal stages (Fig. 11). Our results regarding the occurrence and geochemistry of titanite and pyrite provide insights into the melt/fluid composition, the conditions under which they formed, and the magmatic-hydrothermal processes in the monzonite system.

Magmatic Ttn1 formed as discrete euhedral grains intergrown with K-feldspar, magnetite, and quartz. This assemblage indicates that the monzonitic magma crystallization occurred at a relatively high oxygen fugacity and H_2O -rich environment (Frost and Lindley 1992; Piccoli et al. 2000; Xiao et al. 2021). The high oxygen fugacity is supported by the negative Eu anomaly of Ttn1. High-oxygen fugacity and H_2O contents could lead to a preferential transfer of Au into the magma from its source (Botcharnikov et al. 2011; Wang et al. 2020), resulting in Au enrichment, which is reflected by two analyses of magmatic Py1 that showed relatively high Au contents (0.1 and 0.14 ppm). Because the Nd isotopes of Ttn1 and S isotopes of Py1 are proposed to be likely the result of mixing between magmas from lower crust and lithospheric mantle, the Au could be derived from both sources (Fig. 11a).

In the later hydrothermal stages, fluids were directly exsolved from the late-stage monzonitic magma. The complex textures and geochemistry of Ttn2 and Ttn3 suggest that formation of these minerals was a dynamic process involving different hydrothermal stages (Fig. 11b). The initial hydrothermal fluid was characterized by high-REE contents (especially LREE), which resulted in backscatter bright cores of Ttn2. With further degassing, the hydrothermal fluid precipitated backscatter gray rims of Ttn2 with moderate REE contents (e.g., Fu et al. 2016; Xiao et al. 2021), as well as Py2 with relatively high metal contents (Co, As, Ag, Au, Sb, and Bi). This implies that Au, together with Co, As, Ag, Sb, and Bi, were pre-enriched in the monzonitic magma and were furthermore favorably partitioned into the exsolved fluids

(Pokrovski et al. 2013). In the late hydrothermal stage, the fluid became less oxidized as shown by the variable negative-positive Eu anomalies ($\text{Eu}_\text{N}/\text{Eu}_\text{N}^* = 0.2\text{--}1.1$, average 0.6) of Ttn3—and contained lower total REE contents. The Ttn3 precipitated at this stage overgrew on the rims of Ttn2, and partly penetrated into Ttn2 (Fig. 11b). The pyrrhotite grains were likely precipitated during the late hydrothermal stages (Fig. 11b), due to the consumption of sulfur by deposition of Py2 and less oxidizing conditions. Multiple stages of hydrothermal fluid exsolution from the monzonitic magma show the same Nd and S isotopic compositions. The hydrothermal fluids led to distinct alteration in the biotite monzonite, including silicification, sericitization, and carbonation. We surmise that these same fluids then migrated along faults and fractures, forming quartz-pyrite (Py3) veins in the overlying Luanjiahe granite.

A potential magmatic-hydrothermal model for the Jiaodong Au mineralization

The source(s) of ore-forming fluids and Au, the mechanism(s) for Au enrichment, and the genetic model for the Jiaodong Au deposits have long been debated (Fan et al. 2003; Zhai et al. 2004; Chen et al. 2005; Goldfarb and Santosh 2014; Zhu et al. 2015; Deng et al. 2020b). The possible sources for the ore components include: (1) a crustal source from Precambrian metamorphic rocks and/or Mesozoic granite (Chen et al. 2005); (2) a subcrustal source from volatile- and Au-fertilized metasomatized mantle lithosphere (Zhu et al. 2015; Deng et al. 2020a, 2020b); or (3) a mixed crustal plus mantle source (Zhai et al. 2004). Various models have been postulated to explain the nature of Au mineralization in different settings, including the orogenic Au deposits (Zhou et al. 2002; Goldfarb and Santosh 2014), intrusion-related Au deposits (Sillitoe and Thompson 1998; Nie et al. 2004), magmatic-hydrothermal Au deposits related to mafic dikes (Wang et al. 2020), decratonic Au deposits (Zhu et al. 2015), and “Jiaodong-type” Au deposits (Deng et al. 2015; Li et al. 2015). All these genetic models have advantages and problems, which have been reviewed by Deng et al. (2020b), and are still highly contentious. One critical factor hindering universal acceptance of a single model is the uncertainty of genetic relationship between magmatism and Au mineralization. Ultimately, this uncertainty is underpinned by the question of whether exsolution and degassing of auriferous magmatic-hydrothermal fluid took place. The information provided by magmatic-hydrothermal titanites and pyrites in this study highlights the exsolution of auriferous hydrothermal fluids from the monzonitic magma, and thus supports a magmatic-hydrothermal model for the genesis of the Jiaodong Au province, as discussed below.

Titanite and monazite that formed from the monzonitic magma (Ttn1) and exsolved hydrothermal fluids (Ttn2, Ttn3, and monazite) yielded consistent U-Pb ages (121–118 Ma) overlapping within error with the large-scale Au mineralization age at Jiaodong (120–119 Ma; Ma et al. 2017; Li et al. 2018; Yang et al. 2018; Deng et al. 2020a; Zhang et al. 2020). Spatially, the biotite monzonite intruded at depth beneath the Linglong goldfield, and it is connected with the surface and Au deposits by the Zhaoyuan-Pingdu fault, which hosts hundreds of auriferous quartz veins (Fig. 2b). Hence, our results suggest that the monzonitic magmatism and its accompanying

hydrothermal fluids were both temporally and spatially linked to the Au mineralization. Magmatic pyrite (Py1) from the monzonite has relatively high Au contents (up to 0.14 ppm), suggesting that the magma was fertile for Au. Hydrothermal fluids precipitating Py2 have higher Au contents, as reflected by the presence of submicrometer inclusions of Au and Bi in Py2, again corroborating a genetic relationship with the Au mineralization. Quantitatively, the biotite monzonite may be part of a large-scale magmatic event at ca. 121 Ma in the Jiaodong Au province, consistent with contemporaneous intermediate-felsic rocks, including the Gushan granite located ~35 km to the southwest of the drill core (120–119 Ma; Li et al. 2012b), the widespread intermediate-mafic (130–120 Ma; Ma et al. 2017; Wang et al. 2020) and felsic dikes (123–118 Ma; Li et al. 2019b). Extensive magmatism has the potential to produce hydrothermal fluids forming giant Au deposits. Although many researchers proposed that the ore-forming fluids were sourced from the volatile-enriched metasomatized mantle lithosphere (e.g., Goldfarb and Santosh 2014; Deng et al. 2015, 2020a, 2020b), analyses of mantle xenoliths have suggested relatively low-Au contents of the metasomatized mantle lithosphere (Wang et al. 2020), casting doubt on that interpretation. Wang et al. (2020) underscored the high-Au contents of hydrous magmas that were sourced from the metasomatized mantle. These findings consistently reveal a genetic relationship between biotite monzonite, which potentially involves mantle components and Au mineralization in the Jiaodong Au province.

Previous studies have established that the Jiaodong Peninsula experienced a transition of tectonic regime from regional compression to *trans*-pression or *trans*-tension prior to peak extension since 125–120 Ma, as a far-field response to the change of subduction direction and roll-back of the paleo-Pacific Plate (Sun et al. 2007; Yang et al. 2018; Deng et al. 2020b). The mantle lithosphere under the eastern NCC at this stage had been metasomatized during Triassic and Late Jurassic to Early Cretaceous subduction events (Chen et al. 2005; Liang et al. 2019; Deng et al. 2020a, 2020b). The extension-induced thinning of lithosphere and accompanying asthenospheric upwelling at 130–120 Ma (Zhai et al. 2004; Li et al. 2019a; Wu et al. 2019) triggered partial melting of the metasomatized mantle lithosphere and the lower crust of the NCC, producing hydrous mafic and felsic magmas, respectively (Fig. 11a). These magmas probably extracted Au efficiently from their sources (Wang et al. 2020). Distinct degrees of mixing occurred between the mafic and felsic magmas, forming the biotite monzonite and Gushan granite (Fig. 11a), with distinct ranges of $\epsilon_{\text{Nd}}(t)$, which likely represent two different intrusives formed by the same magmatism. Attributing to the more involved mafic magmas, higher $\epsilon_{\text{Nd}}(t)$ values were yielded in the biotite monzonite than the Gushan granite. With further magmatic evolution, hydrothermal fluids were exsolved from these crystallizing magmas (Fig. 11a), preferentially concentrating Au, As, Sb, Bi, S, Cl, and C into the fluids by a factor of hundreds (Pokrovski et al. 2013). The auriferous fluids ascended along the translithospheric faults into second-order fault systems and precipitated gold, quartz, and sulfides. This model favors a magmatic-hydrothermal origin and explains the intimate spatial and temporal association of Au deposits with mafic-felsic magmatism.

IMPLICATIONS

The biotite monzonite buried in the Linglong goldfield formed at ca. 121 Ma based on titanite U-Pb dating. It displays distinctive petrographic features indicative of hydrothermal alteration and mineralization, as well as containing ubiquitous magmatic-hydrothermal titanite and pyrite. Three types of titanite with different textures and geochemical characteristics were identified, including magmatic Ttn1 with oscillatory and sector zoning under BSE, and hydrothermal Ttn2 and Ttn3, which show core-rim or irregular textures, and higher Fe, Mn, REE, HFSE, but lower Ti, Ca contents than Ttn1. Hydrothermal fluids that precipitated Ttn2 and Ttn3 were sourced from the monzonitic melt that crystallized Ttn1, evidenced by similar chondrite-normalized REE patterns, indistinguishable Nd isotopes [$\epsilon_{\text{Nd}}(t) = -14.7$ to -12.9] and U-Pb ages (120.7 ± 3.1 Ma for Ttn1, 120.9 ± 2.6 Ma for Ttn2 and Ttn3).

Four types of pyrite were analyzed, including magmatic Py1 from the fresh biotite monzonite, hydrothermal Py2 from the altered biotite monzonite, hydrothermal Py3 from the quartz-pyrite veins, and magmatic Py4 from the mafic enclaves of the Gushan granite. The Py1 and Py4 have low concentrations of trace metals, while the Py2 and Py3 have high-Co, As, Ag, Au, Sb, and Bi contents, which correspond to fertile hydrothermal fluids. Magmatic Py1 has broadly similar $\delta^{34}\text{S}$ values (+1.9 to +6.3‰) as Py4 (+5.0 to +6.4‰) but is relatively lighter than hydrothermal Py2 and Py3 (+6.4 to +9.5‰), consistent with sulfur isotopic fractionation between melt and fluid. U-Pb dating of monazite (118.2 ± 4.6 Ma) from the quartz-pyrite veins indicates that the auriferous hydrothermal fluids are synchronous to the monzonitic magma.

In this contribution, evidence from the titanite and pyrite corroborate the exsolution of fertile hydrothermal fluids from the monzonitic magma, suggesting a magmatic-hydrothermal genetic model for the giant Jiaodong Au mineralization. We infer that primary Au was efficiently extracted from the metasomatized mantle lithosphere and the lower crust of the NCC by hydrous magmas at ca. 120 Ma.

ACKNOWLEDGMENTS AND FUNDING

We thank Dapeng Li and Guijun Wen for their help during fieldwork, Lihui Jia, Jiakang Kong, and Zheng Liu for their technical support in running the EPMA, LA-ICP-MS, and LA-MC-ICP-MS analyses. We are grateful to two anonymous reviewers for their constructive feedback that helped to improve an earlier manuscript, and associate editor Paul Tomascak for valuable suggestions and efficient editorial handling. This work was funded by the National Natural Science Foundation of China (no. 42002078), China National Postdoctoral Program for Innovative Talents (no. BX20190327), and China Postdoctoral Science Foundation (no. 2019M660788).

REFERENCES CITED

- Aleinkoff, J.N., Wintsch, R.P., Fanning, C.M., and Dorais, M.J. (2002) U-Pb geochronology of zircon and polygenetic titanite from the Glastonbury Complex, Connecticut, U.S.A.: An integrated SEM, EMPA, TIMS, and SHRIMP study. *Chemical Geology*, 188, 125–147.
- Aleinkoff, J.N., Schenck, W.S., Plank, M.O., Srogi, L., Fanning, C.M., Kamo, S.L., and Bosbyshell, H. (2006) Deciphering igneous and metamorphic events in high-grade rocks of the Wilmington Complex, Delaware: Morphology, cathodoluminescence and backscattered electron zoning, and SHRIMP U-Pb geochronology of zircon and monazite. *Geological Society of America Bulletin*, 118, 39–64.
- Botcharnikov, R.E., Linnen, R.L., Wilke, M., Holtz, F., Jugo, P.J., and Berndt, J. (2011) High gold concentrations in sulphide-bearing magma under oxidizing conditions. *Nature Geoscience*, 4, 112–115.
- Bouvier, A., Vervoort, J.D., and Patchett, P.J. (2008) The Lu-Hf and Sm-Nd isotopic composition of CHUR: Constraints from unequilibrated chondrites and implica-

- tions for the bulk composition of terrestrial planets. *Earth and Planetary Science Letters*, 273, 48–57.
- Cai, Y.C., Fan, H.R., Santosh, M., Liu, X., Hu, F.F., Yang, K.F., Lan, T.G., Yang, Y.H., and Liu, Y.S. (2013) Evolution of the lithospheric mantle beneath the southeastern North China Craton: Constraints from mafic dikes in the Jiaobei terrain. *Geostandards Research*, 24, 601–621.
- Cao, M.J., Qin, K.Z., Li, G.M., Evans, N.J., and Jin, L.Y. (2015) In situ LA-(MC)-ICP-MS trace element and Nd isotopic compositions and genesis of polygenetic titanite from the Baogutu reduced porphyry Cu deposit, Western Junggar, NW China. *Ore Geology Reviews*, 65, 940–954.
- Chen, Y.J., Pirajno, F., and Qi, J.P. (2005) Origin of gold metallogeny and sources of ore-forming fluids, Jiaodong Province, Eastern China. *International Geology Review*, 47, 530–549.
- Chen, L., Li, X.H., Li, J.W., Hofstra, A.H., Liu, Y., and Koehnig, A.E. (2015) Extreme variation of sulfur isotopic compositions in pyrite from the Qiuling sediment-hosted gold deposit, West Qinling orogen, central China: An *in situ* SIMS study with implications for the source of sulfur. *Mineralium Deposita*, 50, 643–656.
- Dare, S.A.S., Barnes, S.-J., Beaudoin, G., Méric, J., Boutroy, E., and Potvin-Doucet, C. (2014) Trace elements in magnetite as petrogenetic indicators. *Mineralium Deposita*, 49, 785–796.
- Deditius, A.P., Reich, M., Kesler, S.E., Utsunomiya, S., Chryssoulis, S.L., Walshe, J., and Ewing, R.C. (2014) The coupled geochemistry of Au and As in pyrite from hydrothermal ore deposits. *Geochimica et Cosmochimica Acta*, 140, 644–670.
- Deng, J., Wang, C., Bagas, L., Carranza, E.J.M., and Lu, Y. (2015) Cretaceous–Cenozoic tectonic history of the Jiaojia Fault and gold mineralization in the Jiaodong Peninsula, China: constraints from zircon U-Pb, illite K-Ar, and apatite fission track thermochronometry. *Mineralium Deposita*, 50, 987–1006.
- Deng, J., Qiu, K.F., Wang, Q.F., Goldfarb, R.J., Yang, L.Q., Zi, J.W., Geng, J.Z., and Ma, Y. (2020a) In-situ dating of hydrothermal monazite and implications on the geodynamic controls of ore formation in the Jiaodong gold province, eastern China. *Economic Geology*, 115, 671–685.
- Deng, J., Yang, L.Q., Groves, D.I., Zhang, L., Qiu, K.F., and Wang, Q.F. (2020b) An integrated mineral system model for the gold deposits of the giant Jiaodong province, eastern China. *Earth-Science Reviews*, 208, 103274.
- Dora, M.L., Upadhyay, D., Randive, K.R., Shareef, M., Baswani, S.R., and Ranjan, S. (2020) Trace element geochemistry of magnetite and pyrite and sulfur isotope geochemistry of pyrite and barite from the Thanewasna Cu-(Au) deposit, western Bastar Craton, central India: Implication for ore genesis. *Ore Geology Reviews*, 117, 103262.
- Fan, H.R., Zhai, M.G., Xie, Y.H., and Yang, J.H. (2003) Ore-forming fluids associated with granite-hosted gold mineralization at the Sanshandao deposit, Jiaodong gold province, China. *Mineralium Deposita*, 38, 739–750.
- Fan, H.R., Hu, F.F., Yang, J.H., and Zhai, M.G. (2007) Fluid evolution and large-scale gold metallogeny during Mesozoic tectonic transition in the Jiaodong Peninsula, eastern China. *Geological Society London Special Publications*, 280, 303–316.
- Feng, K., Fan, H.-R., Hu, F.-F., Yang, K.-F., Liu, X., Shanguan, Y.-N., Cai, Y.-C., and Jiang, P. (2018) Involvement of anomalously As-Au-rich fluids in the mineralization of the Heilan'gou gold deposit, Jiaodong, China: Evidence from trace element mapping and in-situ sulfur isotope composition. *Journal of Asian Earth Sciences*, 160, 304–321.
- Feng, K., Fan, H.R., Groves, D.I., Yang, K.F., Hu, F.F., Liu, X., and Cai, Y.C. (2020) Geochronological and sulfur isotopic evidence for the genesis of the post-magmatic, deeply sourced, and anomalously gold-rich Daluhang orogenic deposit, Jiaodong, China. *Mineralium Deposita*, 55, 293–308.
- Fiege, A., Holtz, F., Shimizu, N., Mandeville, C.W., Behrens, H., and Knipping, J.L. (2014) Sulfur isotope fractionation between fluid and andesitic melt: An experimental study. *Geochimica et Cosmochimica Acta*, 142, 501–521.
- Frost, B.R., and Lindsley, D.H. (1992) Equilibria among Fe-Ti oxides, pyroxenes, olivine, and quartz: part II. Application. *American Mineralogist*, 77, 1004–1020.
- Frost, B.R., Chamberlain, K.R., and Schumacher, J.C. (2001) Sphene (titanite): phase relations and role as a geochronometer. *Chemical Geology*, 172, 131–148.
- Fu, J.L., Hu, Z.C., Zhang, W., Yang, L., Liu, Y.S., Li, M., Zong, K.Q., Gao, S., and Hu, S.H. (2016) In situ, sulfur isotopes ($\delta^{34}\text{S}$ and $\delta^{33}\text{S}$) analyses in sulfides and elemental sulfur using high sensitivity cones combined with the addition of nitrogen by laser ablation MC-ICP-MS. *Analytica Chimica Acta*, 911, 14–26.
- Gilbert, S.E., Danyushevsky, L.V., Rodemann, T., Shimizu, N., Gurenko, A., Meffre, S., Thomas, H., Large, R.R., and Death, D. (2014) Optimisation of laser parameters for the analysis of sulphur isotopes in sulphide minerals by laser ablation ICP-MS. *Journal of Analytical Atomic Spectrometry*, 29, 1042–1051.
- Goldfarb, R.J., and Santosh, M. (2014) The dilemma of the Jiaodong gold deposits: Are they unique? *Geoscience Frontiers*, 5, 139–153.
- Goss, S.C., Wilde, S.A., Wu, F.Y., and Yang, J.H. (2010) The age, isotopic signature and significance of the youngest Mesozoic granitoids in the Jiaodong Terrain, Shandong Province, North China Craton. *Lithos*, 120, 309–326.
- Groves, D.I., Goldfarb, R.J., Gebre-Mariam, M., Hagemann, S.G., and Robert, F. (1998) Orogenic gold deposits: A proposed classification in the context of their crustal distribution and relationship to other gold deposit types. *Ore Geology Reviews*, 13, 7–27.
- Hamilton, P.J., O'Nions, R.K., Bridgwater, D., and Nutman, A. (1983) Sm-Nd studies of Archaean metasediments and metavolcanics from West Greenland and their implications for the Earth's early history. *Earth and Planetary Science Letters*, 62, 263–272.
- Hayden, L.A., Watson, E.B., and Wark, D.A. (2008) A thermobarometer for sphene (titanite). *Contributions to Mineralogy and Petrology*, 155, 529–540.
- Hu, Z.C., Zhang, W., Liu, Y.S., Gao, S., Li, M., Zong, K.Q., Chen, H.H., and Hu, S.H. (2015) Wave[®] signal-smoothing and mercury-removing device for laser ablation quadrupole and multiple collector ICP-MS analysis: application to lead isotope analysis. *Analytical Chemistry*, 87, 1152–1157.
- Jacobsen, S.B., and Wasserburg, G.J. (1980) Sm-Nd isotopic evolution of chondrites. *Earth and Planetary Science Letters*, 50, 139–155.
- Li, J.W., Deng, X.D., Zhou, M.F., Liu, Y.S., Zhao, X.F., and Guo, J.L. (2010) Laser ablation ICP-MS titanite U-Th-Pb dating of hydrothermal ore deposits: a case study of the Tonglushan Cu-Fe-Au skarn deposit, SE Hubei Province, China. *Chemical Geology*, 270, 56–67.
- Li, J.W., Bi, S.J., Selby, D., Chen, L., Vasconcelos, P., Thiede, D., Zhou, M.F., Zhao, X.F., Li, Z.K., and Qiu, H.N. (2012a) Giant Mesozoic gold provinces related to the destruction of the North China craton. *Earth and Planetary Science Letters*, 349–350, 26–37.
- Li, X.C., Fan, H.R., Santosh, M., Hu, F.F., Yang, K.F., Lan, T.G., Liu, Y., and Yang, Y.H. (2012b) An evolving magma chamber within extending lithosphere: an integrated geochemical, isotopic and zircon U-Pb geochronological study of the Gushan granite, eastern North China Craton. *Journal of Asian Earth Sciences*, 50, 27–43.
- Li, L., Santosh, M., and Li, S.R. (2015) The 'Jiaodong type' gold deposits: characteristics, origin and prospecting. *Ore Geology Reviews*, 65, 589–611.
- Li, R.C., Chen, H.Y., Xia, X.P., Yang, Q., Li, L., Xu, J., Huang, C., and Danyushevsky, L.V. (2017) Ore fluid evolution in the giant Marcona Fe-(Cu) deposit, Peru: Evidence from in-situ sulfur isotope and trace element geochemistry of sulfides. *Ore Geology Reviews*, 86, 624–638.
- Li, X.H., Fan, H.R., Yang, K.F., Hollings, P., Liu, X., Hu, F.F., and Cai, Y.C. (2018) Pyrite textures and compositions from the Zhuangzi Au deposit, southeastern North China craton: Implication for ore-forming processes. *Contributions to Mineralogy and Petrology*, 173, 73.
- Li, X.H., Fan, H.R., Hu, F.F., Hollings, P., Yang, K.F., and Liu, X. (2019a) Linking lithospheric thinning and magmatic evolution of late Jurassic to early Cretaceous granitoids in the Jiaobei Terrane, southeastern North China Craton. *Lithos*, 324–325, 280–296.
- Li, X.H., Fan, H.R., Santosh, M., Yang, K.F., Peng, H.W., Hollings, P., and Hu, F.F. (2019b) Mesozoic felsic dikes in the Jiaobei Terrane, southeastern North China Craton: Constraints from zircon geochronology and geochemistry, and implications for gold metallogeny. *Journal of Geochemical Exploration*, 201, 40–55.
- Li, J., Xu, L.L., Bi, X.W., Tang, Y.Y., Sheng, X.Y., Yu, H.J., Liu, G., and Ma, R. (2021) New titanite U-Pb and molybdenite Re-Os ages for a hydrothermal vein-type Cu deposit in the Lanping Basin, Yunnan, SW China: constraints on regional metallogeny and implications for exploration. *Mineralium Deposita*, 56, 441–456.
- Liang, Y.Y., Deng, J., Liu, X., Wang, Q., Ma, Y., Gao, T., and Zhao, L. (2019) Water contents of Early Cretaceous mafic dikes in the Jiaodong Peninsula, eastern North China Craton: Insights into an enriched lithospheric mantle source metasomatized by paleo-Pacific Plate subduction-related fluids. *The Journal of Geology*, 127, 343–362.
- Liu, Y.S., Hu, Z.C., Gao, S., Günther, D., Xu, J., Gao, C.G., and Chen, H.H. (2008) In situ analysis of major and trace elements of anhydrous minerals by LA-ICP-MS without applying an internal standard. *Chemical Geology*, 257, 34–43.
- Liu, S., Hu, R.Z., Gao, S., Feng, C.X., Yu, B.B., Qi, Y.Q., Wang, T., Feng, G.Y., and Coulson, I.M. (2009) Zircon U-Pb age, geochemistry and Sr-Nd-Pb isotopic compositions of adakitic volcanic rocks from Jiaodong, Shandong Province, Eastern China: Constraints on petrogenesis and implications. *Journal of Asian Earth Sciences*, 35, 445–458.
- Ludwig, K.R. (2003) ISOPLOT 3.00: A Geochronological Toolkit for Microsoft Excel. Berkeley Geochronology Center, California, Berkeley, pp 39.
- Ma, W.D., Fan, H.R., Liu, X., Pirajno, F., Hu, F.F., Yang, K.F., Yang, Y.H., Xu, W.G., and Jiang, P. (2017) Geochronological framework of the Xiadian gold deposit in the Jiaodong province, China: implications for the timing of gold mineralization. *Ore Geology Reviews*, 86, 196–211.
- Mao, J.W., Wang, Y.T., Li, H.M., Pirajno, F., Zhang, C.Q., and Wang, R.T. (2008) The relationship of mantle-derived fluids to gold metallogeny in the Jiaodong Peninsula: evidence from D-O-C-S isotope systematics. *Ore Geology Reviews*, 33, 361–381.
- Miao, L.C., Luo, Z.K., Huang, J.Z., Guan, K., Wang, L.G., McNaughton, N.J., and Groves, D.I. (1997) Zircon sensitive high resolution ion microprobe (SHRIMP) study of granitoid intrusions in Zhaoye Gold Belt of Shandong Province and its implication. *Science in China Series D: Earth Sciences*, 40, 361–369.
- Mills, S.E., Tomkins, A.G., Weinberg, R.F., and Fan, H.R. (2015) Implications of pyrite geochemistry for gold mineralisation and remobilisation in the Jiaodong gold district, northeast China. *Ore Geology Reviews*, 71, 150–168.
- Morad, S., El-Ghali, M.A.K., Caja, M.A., Al-Ramadan, K., and Mansurbeg, H. (2009) Hydrothermal alteration of magmatic titanite: Evidence from Proterozoic granitic rocks, Southeastern Sweden. *Canadian Mineralogist*, 47, 801–811.
- Nie, F.J., Jiang, S.H., and Liu, Y. (2004) Intrusion-related gold deposits of North China Craton, People's Republic of China. *Resource Geology*, 54, 299–324.
- Ohmoto, H. (1972) Systematics of sulfur and carbon isotopes in hydrothermal ore deposits. *Economic Geology*, 67, 551–578.
- Olin, P.H., and Wolff, J.A. (2012) Partitioning of rare earth and high field strength ele-

- ments between titanite and phonolitic liquid. *Lithos*, 128–131, 46–54.
- Peterson, E., and Mavrogenes, J. (2014) Linking high-grade gold mineralization to earthquake-induced fault-valve processes in the Porgera gold deposit, Papua New Guinea. *Geology*, 42, 383–386.
- Piccoli, P., Candela, P., and Rivers, M. (2000) Interpreting magmatic processes from accessory phases: titanite—a small-scale recorder of large-scale processes. *Earth and Environmental Science Transactions of the Royal Society of Edinburgh*, 91, 257–267.
- Pokrovski, G.S., Kara, S., and Roux, J. (2002) Stability and solubility of arsenopyrite, FeAsS, in crustal fluids. *Geochimica et Cosmochimica Acta*, 66, 2361–2378.
- Pokrovski, G.S., Borisova, A.Y., and Bychkov, A.Y. (2013) Speciation and transport of metals and metalloids in geological vapors. *Reviews in Mineralogy and Geochemistry*, 76, 165–218.
- Qiu, Y., Groves, D.I., McNaughton, N.J., Wang, L.-G., and Zhou, T. (2002) Nature, age, and tectonic setting of granitoid-hosted, orogenic gold deposits of the Jiaodong Peninsula, eastern North China Craton, China. *Mineralium Deposita*, 37, 283–305.
- Shen, Y.K., Guo, T., Yang, Y.Q., Chen, Z.L., Wei, C.S., and Sun, H.S. (2016) Discovery of biotite monzonite and Ar-Ar thermochronology significance in Linglong gold field. *Journal of Geomechanics*, 22, 778–793 (in Chinese with English abstract).
- Sillitoe, R.H., and Thompson, J.F. (1998) Intrusion-related vein gold deposits: types, tectono-magmatic settings and difficulties of distinction from orogenic gold deposits. *Resource Geology*, 48, 237–250.
- Spandler, C., Hammerli, J., Sha, P., Hilbert-Wolf, H., Hu, Y., Roberts, E., and Schmitz, M. (2016) MKED1: A new titanite standard for in situ analysis of Sm-Nd isotopes and U-Pb geochronology. *Chemical Geology*, 425, 110–126.
- Sun, W.D., Ding, X., Hu, Y.H., and Li, X.H. (2007) The golden transformation of the Cretaceous plate subduction in the west Pacific. *Earth and Planetary Science Letters*, 262, 533–542.
- Tanner, D., Henley, R.W., Mavrogenes, J.A., and Holden, P. (2016) Sulfur isotope and trace element systematics of zoned pyrite crystals from the El Indio Au-Cu-Ag deposit, Chile. *Contributions to Mineralogy and Petrology*, 171, 33.
- Tiepolo, M., Oberli, R., and Vannucci, R. (2002) Trace-element incorporation in titanite: constraints from experimentally determined solid/liquid partition coefficients. *Chemical Geology*, 191, 105–119.
- Wang, Z.C., Cheng, H., Zong, K.Q., Geng, X.L., Liu, Y.S., Yang, J.H., Wu, F.Y., Becker, H., Foley, S., and Wang, C.Y. (2020) Metasomatized lithospheric mantle for Mesozoic giant gold deposits in the North China craton. *Geology*, 48, 169–173.
- Wen, B.J., Fan, H.R., Santosh, M., Hu, F.F., Pirajno, F., and Yang, K.F. (2015) Genesis of two different types of gold mineralization in the Linglong gold field, China: Constraints from geology, fluid inclusions and stable isotope. *Ore Geology Reviews*, 65, 643–658.
- Wiedenbeck, M., Alle, P., Corfu, F., Griffin, W.L., Meier, M., Oberli, F., Quadt, A.V., Roddick, J.C., and Spiegel, W. (1995) Three natural zircon standards for U-Th-Pb, Lu-Hf, trace element and REE analyses. *Geostandards and Geoanalytical Research*, 19, 1–23.
- Wu, F.Y., Yang, J.H., Xu, Y.G., Wilde, S.A., and Walker, R.J. (2019) Destruction of the North China craton in the Mesozoic. *Annual Review of Earth and Planetary Sciences*, 47, 173–195.
- Xiao, X., Zhou, T.F., White, N.C., Zhang, L.J., Fan, Y., and Chen, X.F. (2021) Multiple generations of titanites and their geochemical characteristics record the magmatic-hydrothermal processes and timing of the Dongguashan porphyry-skarn Cu-Au system, Tongling district, Eastern China. *Mineralium Deposita*, 56, 363–380.
- Xie, L., Wang, R.C., Chen, J., and Zhu, J.C. (2010) Mineralogical evidence for magmatic and hydrothermal processes in the Qitianling oxidized tin bearing granite (Hunan, South China): EMP and (MC)-LA-ICP-MS investigations of three types of titanite. *Chemical Geology*, 276, 53–68.
- Xie, S.W., Wu, Y.B., Zhang, Z.M., Qin, Y.C., Liu, X.C., Wang, H., Qin, Z.W., Liu, Q., and Yang, S.H. (2012) U-Pb ages and trace elements of detrital zircons from Early Cretaceous sedimentary rocks in the Jiaolai Basin, north margin of the Sulu UHP terrain: Provenances and tectonic implications. *Lithos*, 154, 346–360.
- Xu, L., Hu, Z., Zhang, W., Yang, L., Liu, Y., Gao, S., Luo, T., and Hu, S. (2015) In situ Nd isotope analyses in geological materials with signal enhancement and non-linear mass dependent fractionation reduction using laser ablation MC-ICP-MS. *Journal of Analytical Atomic Spectrometry*, 30, 232–244.
- Xu, H.J., Zhang, J.F., Wang, Y.F., and Liu, W.L. (2016) Late Triassic alkaline complex in the Sulu UHP terrane: implications for post-collisional magmatism and subsequent fractional crystallization. *Gondwana Research*, 35, 390–410.
- Yang, J.H., and Zhou, X.H. (2001) Rb-Sr, Sm-Nd, and Pb isotope systematics of pyrite: Implications for the age and genesis of lode gold deposits. *Geology*, 29, 711–714.
- Yang, K.F., Fan, H.R., Santosh, M., Hu, F.F., Wilde, S.A., Lan, T.G., Lu, L.N., and Liu, Y.S. (2012) Reactivation of the Archean lower crust: implications for zircon geochronology, elemental and Sr-Nd-Hf isotopic geochemistry of late Mesozoic granitoids from northwestern Jiaodong Terrain, the North China Craton. *Lithos*, 146–147, 112–127.
- Yang, K.F., Jiang, P., Fan, H.R., Zuo, Y.B., and Yang, Y.H. (2018) Tectonic transition from a compressional to extensional metallogenic environment at ~120 Ma revealed in the Hushan gold deposit, Jiaodong, North China Craton. *Journal of Asian Earth Sciences*, 160, 408–425.
- Zhai, M.G., Fan, H.R., Yang, J.H., and Miao, L.C. (2004) Large-scale cluster of gold deposits in east Shandong: anorogenic metallogenesis. *Earth Science Frontiers*, 11, 85–98 (in Chinese with English abstract).
- Zhang, L., Weinberg, R.F., Yang, L.Q., Groves, D.I., Sai, S.X., Matchan, E., Phillips, D., Kohn, B.P., Miggins, D.P., Liu, Y., and Deng, J. (2020) Mesozoic orogenic gold mineralization in the Jiaodong Peninsula, China: A focused event at 120 ± 2 Ma during cooling of pre-gold granite intrusions. *Economic Geology*, 115, 415–441.
- Zheng, Y.F. (2008) A perspective view on ultrahigh-pressure metamorphism and continental collision in the Dabie-Sulu orogenic belt. *Chinese Science Bulletin*, 53, 3081–3104.
- Zhi, Z.Y., Li, L., Li, S.R., Santosh, M., Yuan, M.W., and Alam, M. (2019) Magnetite as an indicator of granite fertility and gold mineralization: A case study from the Xiaqingling gold province, North China Craton. *Ore Geology Reviews*, 115, 103159.
- Zhou, T.H., Goldfarb, R.J., and Phillips, G.N. (2002) Tectonics and distribution of gold deposits in China: an overview. *Mineralium Deposita*, 37, 249–282.
- Zhou, J.B., Wilde, S.A., Zhao, G.C., Zhang, X.Z., Zheng, C.Q., Jin, W., and Cheng, H. (2008) SHRIMP U-Pb zircon dating of the Wulian complex: Defining the boundary between the North and South China Cratons in the Sulu Orogenic Belt, China. *Precambrian Research*, 162, 559–576.
- Zhu, R.X., Fan, H.R., Li, J.W., Meng, Q.R., Li, S.R., and Zeng, Q.D. (2015) Decratonic gold deposits. *Science China Earth Sciences*, 58, 1523–1537.

MANUSCRIPT RECEIVED NOVEMBER 14, 2020

MANUSCRIPT ACCEPTED MARCH 18, 2021

MANUSCRIPT HANDLED BY PAUL TOMASCAK

Endnote:

¹Deposit item AM-22-27889, Online Materials. Deposit items are free to all readers and found on the MSA website, via the specific issue's Table of Contents (go to http://www.minsocam.org/MSA/AmMin/TOC/2022/Feb2022_data/Feb2022_data.html).